5-2016

Validation of a Confocal Light Sheet Microscope using Push Broom Translation for Biomedical Applications

Joshua Hutcheson
University of Arkansas, Fayetteville

Validation of a Confocal Light Sheet Microscope using Push Broom Translation for Biomedical Applications

A thesis submitted in partial fulfillment
of the requirements for the degree of
Master of Science in Biomedical Engineering

by

Joshua A. Hutcheson
University of Arkansas
Bachelor of Science in Biomedical Engineering, 2014

May 2016
University of Arkansas

This thesis is approved for recommendation to the Graduate Council.

_____
Dr. Timothy J. Muldoon
Thesis Director

_____
Dr. Ingrid Fritsch
Committee Member

_____
Dr. Kartik Balachandran
Committee Member

ABSTRACT

There exists a need for research of optical methods capable of image cytometry suitable for point-of-care technology. To propose am optical approach with no moving parts for simplification of mechanical components for the further development of the technology to the poin-of-care, a linear sensor with push broom translation method. Push broom translation is a method of moving objects by the sensor for an extended field of view. A polydimethylsiloxane (PDMS) microfluidic chamber with a syringe pump was used to deliver objects by the sensor. The volumetric rate of the pump was correlated to the integration time of the sensor to ensure images were realistically being formed, termed aspect ratio. An electro-chemical microfluidic system was then also investigated, redox-magnetohydrodynamics (R-MHD), to eliminate the mechanical syringe pump which showed deviations in linear speeds at the specimen plane. To image with adequate signal to background ratio within the deep chamber of the R-MHD device, an epitaxial light sheet confocal microscope (e-LSCM) was used to improve axial resolution. The linear sensor, having small pixels, blocked out-of-plane light while eliminating the need for a mechanical aperture which is used for traditional point-scanning confocal microscopy. The particular linear sensor used has binning modes that were used to vary the axial resolution by increasing the sensor aperture. This approach was validated by using a mirror translated in the axial direction and measuring remitted light intensity. The resulting curve estimated the real axial resolution of the microscope, which compared favorably to theoretical values. The R-MHD and the e-LSCM were then synchronized to perform continuous imaging of fluorescent microspheres and cells in suspension. This study combines epitaxial light sheet confocal microscopy and electro-chemical microfluidics as a robust approach which could be used in future point-of-care image cytometry applications.

ACKNOWLEDGEMENTS

I would like to first, and foremost, thanks my graduate advisor and principal investigator on this project, Tim Muldoon, for his guidance and friendship. Tim has mentored me to be a better writer and presenter through my graduate career, and I hope this thesis reflects his skills that he has imparted to me. I would also like to thank my fellow graduate students, Gage Greening, Amy Powless, and Sandra Prieto, for their proofreading, assistance with experiments, coding help, and friendship. Graduate school is difficult and it was great to have all of you with me. I would also like to acknowledge Foysal Khan and Dr. Ingrid Fritsch for an amazing collaboration and their expertise with redox-magnetohydrodynamic microfluidics; without them, the whole second chapter of this thesis would not be possible. I would like to thank my committee (Dr. Tim Muldoon, Dr. Ingrid Fritsch, and Dr. Kartik Balachandran) for serving on my behalf. I would also like to thank my family for encouraging me to attend graduate school; it has been a great experience. Finally I would like to thank my wife, Hannah Hutcheson, for supporting me through everything. You have been strong for me when I was not, and you have encouraged me when I could not encourage myself.

Table of Contents

LIST OF FIGURES

source code with maximum exposure per line read and 1 x 4 binning. Scale bar represents 50 µm in the x-direction and 1500 µs in time (vertical) direction.

Figure 5. Aspect ratio measurements of the beads in images acquired with a linear imaging camera. The AR tends toward one as the linear translation and line exposure period match. Standard deviations were calculated but were at most 3.69% of the total average value, leaving error bars too small to display. Calculations made in Image J and displayed with MATLAB.

Figure 6. Image of translating fluorescent beads within a microfluidic chamber (500 x 50 µm, Width x Height) acquired at a volumetric pump rate of 16 µl min^{-1} with a line exposure period of 150 µs. Images were taken in 1 x 4 pixel binning mode. Scale bar is 50 µm in x-direction and 1500 µs in the time (vertical) direction.

Figure 7. Image of leukocytes in whole blood taken with the widefield fluorescence microscope with translation speed of 0.22 mm sec^{-1} at a matched line exposure period 1500 µs on a slide. Color bar shows pixel intensity over entire image. Scale bar (a) is 100 µm in x-direction and 30 msec in the time direction. Scale bar (b) is 25 µm in the x-direction and 7.5 msec in the time (vertical) direction.

Figure 8. Images of oral cells taken with the widefield fluorescence microscope with a linear sensor (c-f) compared to an oral cell image taken with a conventional phase contrast microscope (a) and a fluorescence image taken with an area scan sensor on a static platform (b). A nucleus mask and cytoplasm mask (d,e) have been hand-drawn to illustrate the nuclear to cytoplasmic ratio. An

annotated image has been shown (f) (NU: nucleus, CY: cytoplasm, KH: keratohyalin granules) to highlight the subcellular features. Scale bar is 25 µm.

Figure 9. A schematic is shown demonstrating the two interfaced technologies. The e-LSCM light path is shown to be in the epitaxial configuration and the R-MHD is placed at the sample plane. An image is shown of the complete platform as well as an image of the linear sensor.

Figure 10. **(a)** In applied current vs. bead velocity correlation graph bead velocity increases linearly with increasing the current applied between electrodes at two different position (480 µm &1440 µm) of beads in Z direction over the chip. The highest speed for both position at 750 µA obtained are 1395 µm s^{-1} and 1818.33 µm s^{-1} respectively. The least square analysis yield $|V_x| = (2.443 \pm 0.066\ \mu m\ s^{-1}\ \mu A^{-1})\ |i| + (16.35 \pm 32.58\ \mu m\ s^{-1})$ with $R^2 = 0.9971$ for 1440 µm above the chip surface and $|V_x| = (1.842 \pm 0.047\ \mu m\ s^{-1}\ \mu A^{-1})\ |i| + (23.42 \pm 23.14\ \mu m\ s^{-1})$ with $R^2 = 0.9974$ for 480 µm above the chip surface. **(b)** In applied current vs. total flow period correlation graph flow period decreases with increasing the current applied between electrodes. Because a high electronic current (i.e. high speed) uses up charges faster than a low current (i.e. low speed).

Figure 11. The experimental measurements showing the FWHMs are given for 20x (top, left) and 10x (bottom, left). The FWHM are representative of the increase in light throughput, therefore width is inversely related to axial resolution. The values are cited in Table 2.

Figure 12. The qualitative images are shown to demonstrate optical sectioning in a three-dimensional suspension of microspheres in an agarose phantom. The ascending 20x aperture

widths (a-c) show a slight increase in background signal as well as the 10x aperture widths (d-f). A significant increase in background signal is seen between 20x, 0.5 NA and 10x, 0.3 NA demonstrating the significance of numerical aperture in axial resolution. Images were contrast stretched to demonstrate concept. Scale bar is 30 µm.

Figure 13. A graph showing the relationship of applied current to aspect ratio when line period is kept static at 300 µsec. An image is shown for quality assurance of microspheres imaged by e-LSCM in the R-MHD chamber based on the parameters decided in graph. Scale bar is 30 µm.

Figure 14. Images of three types of leukocytes are shown. Cells are stained with acridine orange and suspended in PBS and glycerol. Images were taken in R-MHD chamber with e-LSCM to demonstrate high-resolution imaging of biological samples. Scale bar is 15 µm in the top row. Images of three types of leukocytes stained with the hematopathological standard, Giemsa stain. Scale bar is 10 µm.

SI Figure 1. (a) Microfabricated chip (1 in. X 2 in) design contains four band electrodes where each electrode measured 1.5 cm in length, 650 µm wide and ~100 nm in thickness (b) Current responses during electropolymerization of PEDOT for 12 deposition cycles. It depicts an oxidation peak at 1.3 V of the monomer as well as the growth of the polymer film between the range of -0.5 V and 1.0 V. After 12 successive deposition cycles a dark layer of film deposited on the electrode.

SI Figure 2. (a) Chip connected with edge connector and wires from edge connector goes to bipotentiostat. A PDMS gasket of 2.14 mm placed over the chip to define the cell height. A 0.37 T circular NdFeB magnet used under the chip to provide magnetic flux. (b) MHD setup under

microscope camera. Inset picture shows right hand rule, where net fluid motion $\mathbf{F_B}$ happens when ionic current density **j** and magnetic flux **B** works perpendicular to each other.

SI Figure 3. Current and charge response of PEDOT deposited electrode in 60% Phosphate buffer saline + 40% glycerol solution. Chronoamperometry (CA) was done in order to get maximum current response and chronocoulometry (CC) was done to get charge after 20s.

SI Figure 4**.** Overlay of the current responses for bare electrode and PEDOT modified electrode in 0.1 M KCl solution for only one electrode. The charging current is 813 times higher for PEDOT coated electrode than the bare electrode in 0.1 M KCl solution. This increased charging response allows to sustain fluid flow for longer times with higher speed.

1. Introduction

1.1.Image cytometry

1.1.1. Review of flow cytometry

Cytological characterization or "cytometry" is a broad term for classifying cells toward the purpose of pathological detection and diagnosis of abnormalities in cellular cultures. Cytometry can be separated into automated and manual classification. The manual methods for diagnosis require a trained pathologist to prepare samples, examine and diagnose disease with a classical microscope, but automated classification utilizes machines and algorithms to eliminate the need for manual detection and therefore increasing throughput.

In general, flow cytometry has long been held as the gold standard for automated cytological classification. The throughput of these machines has always been the most attractive feature with capabilities reaching greater than 10,000 cells per second.[1] Flow cytometry uses a capillary tube to siphon cells through the system one at a time to allow the system single cell resolution and passes the cell through laser light causing the cell to emit forward scattering, side scattering or fluorescence. Cell scattering can be used in a limited sense to perform volume (forward scattering) and morphological complexity (side scattering) analysis without the need of contrast agents.[2, 3] The fluorescence emission of the cells are typically elicited by specific markers applied by the scientist or examiner to classify a population (i.e. a dye specific to a cancer cell or a labelling technique that attaches to a specific cell line).[4] Sensors detect these signals and transfer them to a computing unit which provides limited data points per cell, which, again, are constrained to the labelling of the examiner.

At this point in the sample analysis, many, but not all, commercial machines contain a sorting technique to purify sample classifications; one common iteration of this is fluorescence-activated cell sorting (FACS). FACS flow cytometers induce a charge (e.g. positive or negative) on the cell of interest when the optical properties validate its classification. That charge is then attracted by opposing electromagnets to direct the cell into different physical bins based on the charge placed on the cell at optical classification.[5]

The applications of this technology are broad and far reaching. Flow cytometry has been particularly indispensable for monitoring and diagnosing hematopoietic (blood) diseases, especially that of chemotherapy induced myelosuppression. [6, 7] This technique is efficient in this application due to the rapid sample preparation due to the liquid nature of the biological isolate. It has also been useful for head and neck cancers [8] as well as urinary tract metaplasia [9]. These applications are heavily concentrated in cancer monitoring and detection because of the single-cell resolution to detect circulating tumor cells and test adjuvant and neoadjuvant therapies by grading residual disease.[10-12]

Continuous research studies are emerging utilizing flow cytometry techniques toward lab-on-chip technology. The miniaturization and dissemination of this technology to the point-of-care can decrease sample handling and time needed for diagnosis.[13, 14] The lab-on-chip technology can also branch into more personalized tests (e.g. single test or single use chips) while disseminating the technology to developing countries where access to medical personnel and facilities can be limited. Many of these lab-on-chip techniques mimic the single-cell resolution of commercial flow cytometers which can be attractive for rare cell detection applications (e.g. circulating tumor cells)

and cell sorting where purity is of importance (e.g. blood cell types to detect abnormal counts).[15-17] Although flow cytometry is and will continue to be ubiquitous, the limitation of flow cytometry is the lack of image analysis to broaden its classification capabilities. This lack is due to the fundamental design of flow cytometry being a detection based system classifying groups based on fluorescence intensity, electrical impedance, or internal scattering rather than an imaging method.

1.1.2. Motivation and applications in image cytometry

Image cytometry has recently been an interest in research for its combination of flow cytometry and image analysis. The premise of image cytometry is to broaden the impact of current flow cytometry methods by coupling image analysis to track and utilize cell morphological data. Cell morphology can refer to shape, size, subunit expression, distortion, subunit ratio metric analysis, etc. and can be used to not only classify cells but monitor progression of disease.[18, 19] Morphological image features can be used independently or in tandem to design algorithms for morphology tracking within cellular populations. Monitoring progression of disease (e.g. cellular dysplasia) can give researchers a unique look at early and transitional signs of disease and can also help guide decisions on appropriate therapy.

1.1.3. Present and future research in image cytometry

Recent work with image algorithms studying morphology transitions were used to diagnose oral legions as benign, pre-malignant, or malignant growths which decreases the number of biopsies.[20] Another group utilized image analysis by a combination of features in brightfield and darkfield microscopy to classify cells in their particular cell cycle phase based on their imaged

DNA content, this is useful for detecting abnormally proliferating cells which is a hallmark sign of malignancy.[21] Along with algorithms for classification, certain novel imaging techniques have been employed to innovate image cytometry.

1.2.Instrumentation

1.2.1. Modern digital microscopy

Laser scanning microscopy employs ultrafast laser sources and scanning optics (acousto-optical beam deflectors, galvanometer, etc.) to scan over a specimen for image reconstruction in this point-wise fashion. Research has utilized line-scanning beam shapers to excite more of the slide to effectively eliminate a scanning direction. By replacing these point-wise scanners with line-scanning illumination, systems are able to effectively eliminate a dimension of scanning from a two-dimensional scan to a one-dimensional scan.[22-25] Light sheet microscopy (LSM), although not a type of laser scanning microscopy, offers a unique beam shaping technique. [26-28] LSM uses a cylindrical lens that converges a light beam into a two-dimensional sheet of light and demonstrates a linear pattern at the specimen plane. When utilizing a line-scanning illumination technique, work has also been shown coupling this scanning with a linear sensor, often a photomultiplier tube (PMT), so that the emission coupling efficiency is maximized for imaging by matching the sensor shape to the illumination shape. (Figure I1)

1.2.2. Linear sensors in microscopy and commercial applications

A linear CMOS sensor can also, in a similar fashion, maximize throughput efficiency, but it provides on board imaging rather than the signal conversion needed for photomultiplier tubes. Another attractive feature of a linear sensor is its ability to construct images for high-speed

imaging. Linear sensors have been widely applied to image objects in motion to increase imaging throughput. These sensors are attractive to eliminate motion blur of fast moving objects as they acquire lines of a scene at a time, transfer them intermittently to a central computing unit, and concatenate them in post-acquisition.[29] Intermittent data transfer allows these linear sensors to have more rapid acquisition and shorter exposure periods which combats motion blur when imaging rapidly moving objects, while these advantages have been achieved by two-dimensional arrays [30] linear sensors can bypass the extensively complex sensor architecture needed for standard area sensors. The commercial applications of these sensors are wide-stretching, including low-cost high speed imaging, non-contact string vibration detection, solar energy monitoring, and satellite image processing.[31-34]

1.2.3. Confocal fluorescence microscopy

A more specific form of modern digital microscopy that has been proposed coupled with linear sensors is confocal fluorescence microscopy. Confocal fluorescence microscopy, a type of laser scanning microscopy, uses epitaxial illumination so that the excitation light passes through the back aperture and the emission light passes back through the same objective towards the sensor. A slit is needed in line-scanning confocal systems to mask out of focus light and reduce signal from out-of-plane sources. To eliminate the need for a mechanical slit, the small pixel size of image-based sensors has been used as a means to reject out-of-plane light.[23, 25, 35, 36] These sensors essentially act as both the slit as well as the image sensor.

1.2.4. Push broom translation

A need has been expressed to simplify optics for the use of point-of-care dissemination. A line excitation at the specimen plane can be matched with a linear sensor to eliminate a scanning direction while still maximizing light throughput efficiency. Another method that could be used to simplify this modern optical approach is push broom translation.

Push broom imaging is the synchronization of the imaging source (i.e. line exposure of a linear sensor) to image a moving object across the face of the sensor (Figure I2).[37] This technique was made known and it currently widely used by imaging satellites in earth's orbit.[38, 39] The idea of delivering objects (i.e. biological specimens) to the focal plane of a high speed microscopy platform has been explored extensively [40, 41] as well as integrating microfluidics with light sheet microscopy [42] for image cytometry, but the method of synchronizing these two for push broom imaging with a linear sensor at the microscopic level is not well understood.

The proposed system is a combination of the motivated optical developments explained. These developments have the potential to provide innovative optical techniques while employing a simplified instrumentation approach. A cylindrical lens was used to shape a linear excitation to expand the field of view while eliminating a dimension of scanning. A linear sensor was used for fast, intermittent data transfer while also providing maximum signal throughput by matching the excitation pattern. The specific sensor used also allowed for optical sectioning without a pinhole due to precise alignment and small pixels. A push broom translation method was used to eliminate scanning optics and to develop a system that employs microfluidics as a delivery method to eliminate all moving parts. All of these developments combined provide an attractive platform for

further prototypical instrumentation developments for a robust image cytometer at the point-of-care.

1.3.Chapter summary

In the subsequent chapters, an approach will be presented that utilizes push broom translation synchronized to a linear sensor to image objects on a slide or in a microfluidic chamber. Chapter one describes the use of a microscopy system coupled to a linear image sensor to perform high-resolution imaging of cell populations. We describe how linear acquisition timing and sample translation are synchronized to control image distortion. Human leukocytes and oral cells were imaged on a slide translated by the mechanical stage to demonstrate high-resolution imaging of biological specimens while conserving image distortion during push broom translation. Chapter two describes a light sheet microscope coupled with a linear image sensor which acts as a confocal aperture. The push broom translation method demonstrated in this system is a deep well electro-chemical microfluidic chamber called redox-magentohydrodynamic (R-MHD) microfluidics. The two devices were characterized independently and then merged to introduce a proof of concept validation study to demonstrate a more reliable microfluidic platform coupled with a high-resolution biological imaging microscope with no moving parts.

1. CHAPTER 1: A WIDEFIELD FLUORESCENCE MICROSCOPY PLATFORM WTH A LINEAR IMAGE SENSOR FOR IMAGE CYTOMETRY OF BIOSPECIMENS: CONSIDERATIONS FOR IMAGE QUALITY OPTIMIZATION

1.1. Abstract

Linear image sensors have been widely used in numerous research and industry applications to provide continuous imaging of moving objects. Here, we present a widefield fluorescence microscope with a linear image sensor used to image translating objects for image cytometry. First, a calibration curve was characterized for a custom microfluidic chamber over a span of volumetric pump rates. Image data was also acquired using 15 µm fluorescent polystyrene spheres on a slide with a motorized translation stage in order to match linear translation speed with line exposure periods to preserve the image aspect ratio. Aspect ratios were then calculated after imaging to ensure quality control of image data. Fluorescent beads were imaged in suspension flowing through the microfluidics chamber being pumped by a mechanical syringe pump at 16 µl min^{-1} with a line exposure period of 150 µs. The line period was selected to acquire images of fluorescent beads with a 40dB signal-to-background ratio. A motorized translation stage was then used to transport conventional glass slides of stained cellular biospecimens. Whole blood collected from healthy volunteers was stained with 0.02% (w/v) proflavine hemisulfate was imaged to highlight leukocyte morphology with a 1.56 mm x 1.28 mm field of view (1540 msec total acquisition time). Oral squamous cells were also collected from healthy volunteers and stained with 0.01% (w/v) proflavine hemisulfate to demonstrate quantifiable subcellular features and an average nuclear to cytoplasmic ratio of 0.03 (n = 75), with a resolution of 0.31 µm $pixel^{-1}$.

1.2. Introduction

Linear image sensors comprised of single or consecutive row(s) of active pixels- as opposed to a two-dimensional array as in area-scan cameras- are used in myriad industrial applications. These include quality control conveyor belts, fax machines, scanners, high-resolution document scanning, and raw material surface inspection.[43-46] The advantages of linear imaging systems include a reduced sensitivity to motion blur and short frame read times when compared to frame transfer times of conventional area-scan cameras, providing continuous coverage of the translating region of interest.[29] Two-dimensional images can be acquired using linear image sensors by translating the region of interest or the sensor itself. While extremely high-speed area-scan cameras have been demonstrated and are commercially available, linear imaging cameras offer similar line rates without the need for unique or extensive data transfer hardware.[47] Linear image sensors with sufficiently fast line transfer rates may be used to significantly reduce image blurring artifacts when directly imaging moving objects.[29, 48-51] Controlling line transfer rate and translation speed are critical to minimize distortion in image aspect ratio. In fluorescence applications, where relatively low intensity emission light is produced, direct imaging methods are challenging, as the requirements for adequate signal-to-noise (long sensor integration times) work against the requirements for limiting motion blur (fast frame rates). As in any high-speed imaging applications, short line transfer rates limit the allowable integration time which may be detrimental to low-light imaging applications. Despite this limitation, continuous image acquisition and the reduction in motion blur when imaging objects moving at high speed relative to the sensor makes linear imaging cameras attractive for designing high-throughput imaging-based applications.

Linear image sensors have been previously used in a number of research areas. These applications may utilize the linear sensor to improve frame rates during laser scanning microscopy applications,

for acquiring spectrally-encoded data in the case of OCT or hyperspectral imaging, or to image moving objects with the aid of a translating stage. Some notable areas include confocal imaging, hyperspectral imaging, optical coherence tomography (OCT), and multi-photon microscopy.[52-56] Along with these, transmission white light microscopy is a platform that has been interfaced with a linear sensor and translating stage; this method utilized a low-cost linear CMOS sensor and a conventional microscope to reduce imaging time.[57, 58] Another benchtop platform is a stage-scanning line confocal microscope with the ability to image brain neuron connectivity; this microscope yielded images of a 10 x 10 mm^2 coronal plane in 88 seconds with a resolution of 0.16 µm $pixel^{-1}$.[59] Another approach utilized a translating stage and a continuous-motion time-delay-and-integrated scanning; this custom translation stage exhibited multiple focal depths which was used to show the automated focusing ability with continuous scanning acquisition.[60]

Microfluidics is a broad, active area of research across numerous disciplines. Custom microfluidic chips are used in a variety of biomedical applications to contain, transport, and label biospecimens for imaging and analysis. Recent advances in microfluidic platforms based in labeling and measuring biospecimens include cell impedance measurement, on-chip mixing, 3D holography and lensless imaging.[61-65] This application is also a means of linear translation that can be used as an alternative to scanning technologies that move the imaging hardware. A microfluidic application more specifically focused in the transportation of specimens is magnetohydrodynamics. This application utilizes forces governed by the Lorentz equation and is seen by many to be a reliable method for precise fluid control.[66, 67] Transportation of large numbers of bacteria, cells, microparticles, and other micron-scale structures obviates the need for high speed sensing and reporting mechanisms.

In this manuscript, we present and characterize a fluorescence microscopy platform which uses a Camera Link-based high-speed linear CMOS camera for image cytometry. We demonstrate distortion-free imaging of cell-size fluorescent microspheres pumped in a microfluidic chip, and the ability to image leukocytes stained in whole blood and stained oral cells on a slide with a linear translation stage.

1.3. Materials and Methods

1.3.1. Imaging system

The imaging system was based on an epi-illumination fluorescence microscope which may be used in an inverted or upright configuration. Imaging was performed with the linear imaging camera image sensor perpendicular to the direction of flow (Figure 1). Illumination was provided by an LED (LEDSupply, USA) with a center wavelength 455 nm; a filter cube utilizing a 455 / 25nm FWHM bandpass excitation filter, dichroic mirror with a cutoff wavelength of 475 nm and a 515 / 25 nm bandpass emission filter (Chroma Technologies, USA) was used to deliver excitation light to the back aperture of the objective. The 20x infinity-corrected objective lens (Nikon, Japan) featured a numerical aperture (NA) of 0.5 and a working distance (WD) of 2.1 mm. Fluorescence emission light was collected by the objective, passed through the dichroic and emission bandpass filter, and was focused onto the image sensor using a 150 mm achromatic doublet which served as the tube lens in this infinity-corrected configuration.

The imaging camera was the ELiiXA+ 8k/4k monochrome linear imaging camera (e2v, France) which features a 4 line sensor array of 8192, 5 μm square pixels. The sensor has six, 2-dimensional pixel binning modes that offer a variety of different effective pixel sizes. Binning can be used to increase the effective pixel size by combining adjacent pixels. The binning mode used in this

manuscript was 1 x 4, yielding an effective pixel size of 5 μm x 20 μm. The ELiiXA+ used displays a maximum line rate of 40 kHz, and data transfer via Camera Link to a PCI Express frame grabber (Bitflow, Inc., USA). Camera acquisition was controlled by Image Acquisition Toolbox and a custom MATLAB code to concatenate the images into a one-dimensional time-based array (Mathworks, USA), and all images were acquired in 8-bit.

1.3.2. Microfluidic fabrication and linear speed characterization

To demonstrate microfluidics imaging with a linear sensor, a single channel was constructed via conventional soft lithography methods. The channel was designed to exhibit a tear drop shape at 16º grade to the normal at the entry and exit ports surrounding the straight portion of the channel. This design was printed onto a stencil (CAD / Art Service Inc., USA). The print was then used to graft the chambers onto a silicon wafer (University Wafers, USA) by a modified protocol (Nippon Kayaku Co. MicroChem, USA). The chambers were grafted of poly(dimethylsiloxane) (PDMS) (Dow Corning, USA) from this silicon wafer with a modified protocol.[68] After curing the chamber and plasma activating its surface, it was sealed with a #2 coverslip (22 x 60 mm, VWR International, USA) for direct imaging into the microfluidics device (Figure 2). Holes (3.18 mm diameter) were punched in the under-side of the chamber for inlet and exit ports. Tubing was connected to the ports for fluid transport. The pump used laboratory clear, tygon PVC tubing (1.59 mm ID, 3.18 mm OD, McMaster Carr, USA) to pump into the chamber as seen in Figure 2. The tubing and syringe were connected by barbed-socket coupling adapter (1.59 mm barb OD, McMaster-Carr, USA); this barb fit the inner diameter of the tubing.

To characterize the microfluidics device, we collected images of fluorescent microspheres in a time-series using an epi-illumination fluorescent microscope with a 20x objective with 0.50 NA

and 2.1 WD with a Flea3 monochrome area-scan camera (Point Grey, Canada) focused on a 260 x 190 μm field of view. This area-scan camera was capable of imaging and tracking extremely bright polystyrene fluorescent beads, but not fluorescently stained cells at high translation speeds (see section D). This camera was used to more conveniently track individual beads over time to calculate linear translation speed in the microfluidic channel. To prepare the bead suspension, beads were spun out of solution and supernatant removed. They were then re-suspended in 70% 1x phosphate buffered saline (PBS) solution (Sigma-Aldrich, USA) and 30% 50/50 glycerol (Sigma-Aldrich, USA) in deionized water to keep the beads suspended in solution at neutral buoyancy.

The bead suspension was introduced into the microfluidics chamber at a set volumetric rate with a programmable, mechanical syringe pump (BS-8000 120V, Braintree Scientific, USA). As beads moved through the field of view the acquisition software was set to acquire images every 50 msec with 5 msec integration time and 3 dB gain. Images were imported into Image J (Broad Institute, USA) to process the speed of the beads along the interval that the acquisition occurred. Bead movement was counted by interval spanned from frame to frame rendering a pixel per millisecond speed and converted to millimeters per second based on the magnification of the imaging system. The coinciding translation speeds were then plotted on a reference curve.

1.3.3. Line rate calibration to minimize image distortion

The linear flow speeds from the reference curve (Figure 3) were used as a guide to experimentally determine the ideal line read time to minimize image distortion. Data was acquired at 150 μs line exposure period while linear translation speeds ranged from 0.5 mm sec^{-1} to 3.4 mm sec^{-1}. This line exposure period was chosen to yield a desirable signal to background ratio of 40 dB. To more

precisely control linear speed, 15 µl of beads were placed on a slide with a #2 coverslip and translated with a motorized linear stage (Thorlabs, USA). Image acquisition was set to maximum exposure per line and 1 x 4 pixel binning yielding an effective pixel size of 5 x 20 µm. Ten beads were randomly selected from data sets measured between 0.5 mm sec^{-1} and 3.4 mm sec^{-1} to measure the speed's effect on aspect ratio. The aspect ratio was defined as the ratio of the objects height to its width (Figure 5). Images were taken in IMAQ toolbox with a custom MATLAB code and measurements were taken manually in Image J on the specific scale of magnification.

1.3.4. Imaging fluorescent beads in a microfluidic chamber

To perform microfluidics imaging, beads were suspended in a 100 µl solution of glycerol and PBS (70/30 PBS to 50% glycerol in DI water), then introduced to a 500 x 50 µm (Width x Height) channel. Images were acquired in 1x4 binning mode yielding 8192 x 5120 two-dimensional images. The beads were pumped at 16 µl min^{-1} and imaged with a 150 µs line exposure period.

1.3.5. Whole blood preparation and imaging

All blood samples were obtained following informed consent of a healthy volunteer in accordance with an IRB protocol (#13-06-759) at the University of Arkansas. The subject's index finger was first wiped with an alcoholic swab for a sterile location. The finger was then pricked with a diabetic lancet (ReliOn, USA) and gently squeezed to maximize blood collection. The 20 µl sample was then taken directly off of the finger-tip via a sterile micro-pipette and added to a microcentrifuge tube containing 12 µl heparin (2 IU mL^{-1}, Sigma-Aldrich, USA). A 20 µl solution of 0.02% (w/v) proflavine hemisulfate was added to the heparinized blood. Proflavine is an acridine-derived dye which is known to intercalate DNA, preferentially labeling only leukocytes.[69] A small volume

of this solution (10-20 µl) was then placed on a histology slide (VWR International, USA) and covered with a #1 coverslip (22 x 40 mm, VWR International, USA) to be imaged on a motorized linear translation stage.

1.3.6. Oral cell preparation and imaging

All oral squamous cell samples were obtained following informed consent of a healthy volunteer in accordance with an IRB protocol (#13-06-759) at the University of Arkansas. A solution at 5:1 dilution of 0.01% (w/v) proflavine hemisulfate and 50% Glycerol (Sigma Aldrich, USA) in deionized water, respectively, was prepared for fluorescent staining. The subject's mouth was then swabbed with a cotton swab (VWR International, USA) and added to the prepared solution. A 20 µl drop of solution was added to a histology slide (VWR International, USA) and covered with a #1 coverslip (22 x 40 mm, VWR International, USA) to be imaged on a motorized linear translation stage.

The images were imported into Image J post-acquisition to calculate nuclear to cytoplasmic ratio (N:C ratio). A trace was hand drawn around the border of the cell and then around the border of the nucleus. The nucleus size was then subtracted from the value of the entire cell to calculate the size of the cytoplasm. N:C ratio was then calculated for each cell.

1.4. Results

1.4.1. Microfluidic characterization

The volumetric pump rate was varied to calculate the corresponding linear flow rate to develop a best fit line and reference curve (Figure 3). Volumetric pump rates were chosen from 6.6 µl min^{-1} to 36.6 µl min^{-1} yielding linear translation speeds from approximately 0.5 mm sec^{-1} to 5.5 mm

sec^{-1}. An empirical equation was derived where x is the volumetric pump rate and f(x) is the linear translation speed.

1.4.2. Line rate calibration

Aspect ratio is defined as the actual shape of the object of interest and is measured as the bead height to width. As the translation speed and line exposure period is matched the aspect ratio tends toward 1. In Figure 4, proof-of-concept is demonstrated where beads were translated at 1.0, 2.3, and 3.4 mm sec^{-1} and the line read time was 150 μs in each image.

Ten beads were randomly selected at each speed along 11 speeds between 0.5 mm sec^{-1} and 3.4 mm sec^{-1} to measure aspect ratio. Line exposure period was 150 μs per line. These measurements and standard deviations were calculated and plotted (Figure 5); maximum values were 3.69% of the total average value leaving error bars too small to display at the scale shown. The aspect ratio tends toward 1 as the line rate and translation speed are matched because the height and width of the sphere match as a circle. The aspect ratios are greater than one when the camera acquires too quickly for the translating objects and appear stretched. The objects appear compressed and have an aspect ratio tending toward less than 1 as they move quicker than the camera is set to acquire. The ideal linear translation speed for 150 μs line exposure period was determined to be 2.2 mm sec^{-1}, since the calculated aspect ratio tended toward a value of 1; this had a calculated 1.64% standard deviation from the average value. An empirical equation was derived where x is linear translation speed and f(x) is aspect ratio.

1.4.3. Linear imaging in a microfluidic chamber

The reference values of linear translation speeds (Figure 3) and matching line exposure periods (Figure 4), were then applied to acquire image data of moving fluorescent beads in suspension in a microfluidic chamber. The sensor effectively gathered 153.6 msec of data per frame with a 2.05 mm lateral field of view. A cropped view is presented in Figure 6 to quantify distortion. The image data from Figure 6 were then imported to Image J where aspect ratios were manually calculated, with the same protocol previously described; results are shown in Table 1.

TABLE I. Aspect ratio of in-focus beads in microfluidic chamber

Beads	*Height*	*Width*	*Aspect Ratio*
1	14.391	14.796	0.9726
2	15.353	15.202	1.0099
3	14.138	14.138	1.0000
4	15.050	14.898	1.0102

1.4.4. Whole blood imaging

Images of leukocytes stained in whole blood were acquired to demonstrate high-resolution image cytometry capability. The original image rendering Figure 7 was 6248 x 5120 pixels showing a field of view that is 1.56 mm x 1.28 mm (1540 msec total acquisition time) corresponding to a line exposure period of 1500 µs. This line exposure period was decided based on an approximation that leukocytes provide a 10:1 decrease in fluorescence signal compared to polystyrene microspheres; so to obtain a similar signal to background ratio the line exposure period was increased by 10 times and linear translation was decreased to 0.22 mm sec^{-1}. The first image (Figure 7 (a)) was then cropped to 1920 x 1920 pixels for reasonable display resolution; this is a

.588 x .588 mm (30 msec acquisition time) field of view. A 0.132 x 0.119 mm (7.5 msec acquisition time) field of view within the raw image was then cropped to display cell features (Figure 7 (b)).

1.4.5. Oral cell imaging

Images of oral cells were acquired to exhibit further quantifiable metrics toward a multi-functional image cytometry platform (Figure 8). A phase contrast image is shown for a proof of concept comparison to a common microscopy platform; along with an area scan image of an oral cell on a slide stained with 0.01% (w/v) proflavine to exhibit the robust signal of the stain (Figure 8 (b)), but also a comparison of area scan and line scan imaging. An example is also shown of the calculation of N:C ratio (Figure 8 (d,e)). The N:C ratio was calculated at an average of 0.03 au. (n = 75 cells). Images were cropped to display subcellular features (NU: nucleus, CY: cytoplasm, KH: keratohyalin granules) as highlighted in Figure 8. (f). Images were acquired at 1500 µs line exposure period and a 0.22 mm sec^{-1} linear translation; this was done to obtain a signal to background ratio similar to that of fluorescent beads.

1.5. Discussion and Conclusion

The simple microfluidics chamber shown in Figure 2 features a set depth of 50 microns. In higher resolution objective lenses (40x, 0.8 NA and above, for example), the narrow depth of focus may yield some out-of-focus objects when these objects are sufficiently smaller than the chamber height. In Figure 3, there is a fitting trend line to the linear translation speeds measured at different volumetric pump rates. Future work and refinement of this technique will produce more consistent translation speeds to preserve aspect ratios. The preservation of this aspect ratio is critical to image as demonstrated in Figure 4. Figure 5 shows the expected trend of decreasing aspect ratio as

translation speed is increased. Further studies could be done on the allowable standard deviation of aspect ratio for effective post-acquisition analysis. The beads imaged in the microfluidic chamber (Figure 6) maintained aspect ratio as seen in the measurements of Table 1, but had inconsistent depths of focus due to the size of the beads being significantly less than that of the chamber height, which was previously mentioned. An additional constraint must be considered when imaging whole blood specimens as seen in Figure 7; the line exposure period was increased as the signal was lower due to a relatively low fluorescence yield, which significantly increased the imaging time. While higher numerical aperture objective lenses are capable of collecting more emission light, the trade off with a more narrow depth of focus may yield out-of-focus objects. Images shown in Figure 8 were a part of a larger data set to determine an average N:C ratio which is a common dysplastic marker. [70, 71]

We have demonstrated a widefield fluorescent microscope with a linear image sensor as a means to image moving objects while minimizing motion blur. An ideal translation speed at a desired line exposure period was determined as a reference value to conserve image aspect ratio. Images were then acquired of leukocytes in whole blood and oral cells stained with proflavine hemisulfate to demonstrate high-resolution image cytometry capability.

Future iterations of this method could be applied to investigate biospecimens such as whole blood and epithelial swabs for cytomorphology data based on image feature calculation.[72] The wide field of view demonstrated by the linear image sensor enables collection of large numbers of discrete cell images in relatively short periods of time. Data mining methods may be applied to these large data sets to extract useful information about cell behavior, differentiation, morphology, or other diagnostically useful parameters for a wide variety of applications in clinical medicine and biomedical and biological research.

2. CHAPTER 2: REDOX-MAGNETOHYDRODYNAMIC CONTROLLED FLUID FLOW WITH POLY (3, 4-ETHYLENEDIOXYTHIOPHENE (PEDOT) COUPLED TO AN EPITAXIAL LIGHT SHEET CONFOCAL MICROSCOPE TOWARD IMAGE CYTOMETRY APPLICATIONS

2.1. Abstract

A need exists for an image cytometer with continuous field of view and limited reagent preparation. We present two merged technologies to perform continuous push broom imaging in a deep microfluidic chamber. An epitaxial light sheet confocal microscope (e-LSCM) was used to image, with redox-magnetohydrodynamic (R-MHD) as pumping system for precise control of fluid flow. Poly (3, 4 ethylenedioxythiophene) (PEDOT) electrodeposited on MHD chip as immobilized redox species. The e-LSCM was validated to optically section with an electronically adjustable linear aperture by an optical phantom of agarose and suspended fluorescent polystyrene microspheres. The R-MHD pumping was characterized to specific linear speeds as a function of applied current. The linear speed within the chamber and the camera linear exposure periods were synchronized to ensure quality image acquisition. Images of leukocytes stained with acridine orange, an amphipathic vital dye that intercalates DNA, were then taken in the R-MHD chamber with the e-LSCM to demonstrate high-resolution capabilities of biological samples. The combination of these technologies provides a platform for large sample volumes without clogging due to a deep chamber and high concentrations due to optical sectioning. We present these results as a proof-of-concept toward quantifying a broad range of cellular populations.

2.2. Introduction

Flow cytometry provides population-based data for large quantities of single cells, providing information such as light scattering and fluorescence intensity on a cell-by-cell basis. However, flow cytometry suffers a limited classification method; this is due to the relative difficulty of acquiring high-resolution images of cells while simultaneously achieving comparable sampling rates. Image cytometry has long been an established method to confront this insufficiency by merging high resolution imaging with comparable high-throughput analysis. There have been commercial products that perform this merge but they require extensive sample preparation, do not have the capability of point of care diagnostics, and require single-cell analysis rather than bulk flow.[28] This method, although it can use similar techniques to flow cytometry (e.g. hyperspectral imaging, fluorescent probe detection via cellular biomarkers, etc.), also seeks to provide a more comprehensive data set to differentiate cells with morphological image features. Cellular morphology (shape, size, internal complexity, etc.) is a robust tool to provide additional quantitative data for differentiation of population heterogeneity (subunit expression, dysplastic markers, etc.) while preserving the opportunity for optical methods utilized in conventional flow cytometry.

Recent work with population differentiation include cell-cycle classification, severity of dysplasia, drug risk efficacy, and live-cell shape dynamics.[20, 21, 73, 74] Nuclear segmentation has in particular been popular in histopathology with whole slide scanners and digital histology analysis.[75] Other clinical image cytometry systems exist such as slide scanner used in hematopathology (mention product name here) to directly image prepared slides. Although the current technology is efficient with prepared slides (whole slide scanners) and single cell analysis (flow cytometry), a need exists for a technology toward limit of sample preparation and a broader

range of biological sample compatibility which also has the capability for miniaturization and dissemination to the point-of-care.

Recent developments in MHD microfluidics position this as a viable approach. MHD generates a body force $\mathbf{F_B}$ (N / m^3) in a system where an external magnetic field B (T) works perpendicularly with ionic current density j ($C/s\,m^2$)) originated through applied potential difference by following right hand rule $\mathbf{F_B = j \times B}$.[76, 77] Chemical species added with electrolyte solution supply redox centers into the system which turns MHD into Redox - MHD. It generates sufficient current with low voltage and avoid bubble formation from electrolysis of water.[78] Conducting polymer immobilized on electrode surface is replacing solution redox species to allow least chemical interference, higher initial current, and ease of preparation and use. This finding led to on chip image cytometry where cells in solution will be pumped by R-MHD in between working and combined counter/reference electrodes as a push broom translation mechanism for imaging with the e-LSCM. Push broom imaging with a linear sensor was previously validated as an attractive approach for image cytometry.[79] Recent developments in this approach include the alignment of a light sheet to a linear sensor in an epitaxial configuration. This allows for confocal microscopy and the elimination of a slit or pinhole by placing the linear sensor at the image plane to utilize the small pixels for dual-modal optical sectioning and high resolution imaging.

We propose an epitaxial-light sheet confocal microscope synchronized with a redox-magnetohydrodynamic fluid transport system as an image cytometer. A deep well microfluidic chamber was used to increase linear speeds, increase amount of sample to be held, and eliminate clogging of biological specimens. A linear sensor aligned as a confocal slit aperture utilized optical sectioning to image large fluid samples and dense populations of biological material. PEDOT has

been deposited through non-aqueous route onto the electrodes of R-MHD chip asorganic solvent dissolves EDOT more efficiently without adding any solubilizer, minimizing the sample preparation, induce more effective PEDOT packing, and produce films with enhanced charge density. Fluid transport speeds were precisely control and synchronized with the acquisition speed of a linear sensor in order to maximize data quality. This system has promising applications in the area of image cytometry as the system could potentially be used to rapidly image large amounts of biological specimens.

2.3. Materials and Methods

2.3.1. Chemicals and Materials

All chemicals were reagent grade and used as received. Propylene carbonate (anhydrous 99.7 %) was purchased from Sigma – Aldrich (St. Louis, MO). Lithium Perchlorate (ACS min 95 %) was purchased from Alfa Aeser (Ward Hill, MA). Deionized water from Ricca Chemical Company (Arlington, TX). 3, 4-Ethylenedioxythiophene (EDOT) was purchased from Sigma-Aldrich (St. Louis, MO). Potassium ferricyanide and potassium ferrocyanide were obtained from EM Science, Gibbstown, NJ and J.T. Baker, Phillipsburg, NJ, respectively. Fluorescent polystyrene microspheres were purchased (Life Technologies, Grand Island, New York). 0.37 T NdFeB permanent magnet was purchased from Amazing Magnets, Irvine, CA. Pre-cleaned micro cover glass (24 X 50 mm) purchased from VWR.

2.3.2. Optical instrumentation assembly

The light sheet confocal fluorescence microscope has a laser light source for excitation with a 445 nm wavelength (FTEC2 440-20, Blue Sky Research, Milipitas, CA) coupled to a single mode fiber

to produce a Gaussian output beam. The beam is attached to a collimator (Blue Sky Research, USA) with an output diameter of 1.2-1.3 mm which is then expanded by a custom beam expander; collimation was validated by a shear plate (Thorlabs, Newton, NJ). This expander produces a 10 mm beam which is converged into a sheet of light by a cylindrical lens (Thorlabs, Newton, NJ), reflected by a dichroic mirror with a cutoff of 475 nm, and transmitted through the back aperture of the objective lens. The focal length of the cylindrical lens is aligned to the back aperture of the objective lens in order that it receives emission light at the working distance in the epitaxial position. The fluorescent light then passes through the dichroic mirror and is focused onto a linear image (ELiiXA+ 8k/4k, e2v, Chelmsford, UK) in the conjugate image plane by an achromatic doublet lens (Thorlabs, Newton, NJ) with a focal length of 150 mm. The linear sensor is placed at the image plane and acts as a slit detector with electronically controlled binning modes to modulate the aperture width; this allows this device to optically section without the need of a mechanical slit. The imaging stage is electronically controlled by x, y and z actuators (Thorlabs, Newton, NJ). The entire platform, including the stage, acquisition parameters, and image acquisition, are controlled by a custom graphical user interface in MATLAB. The complete system with a schematic is shown in Figure 9.

2.3.3. Redox-magnetohydrodynamic (redox-MHD) microfluidic chip

Microfabrication procedure and design of the similar types of chip has been reported previously.[80] Each 1 in. x 2 in. chip contains 4 band electrodes (Figure 1a in supplementary information) where each electrode measured 1.5 cm in length, 650 μm wide and ~100 nm in thickness, with 3 mm gaps between the two pairs of outermost electrodes and six sets of concentric ring and disk electrodes varying in size. Only the band electrodes were used for pumping.

2.3.4. Poly(3,4-ethylenedioxythiophene (PEDOT) deposition

PEDOT deposited onto the gold band electrodes by electro polymerizing 3,4 ethylene dioxythiophene (EDOT). Before deposition chip was plasma cleaned for 15 minutes to remove any possible organics from the electrode surface. A propylene carbonate precursor solution containing 0.1 M $LiClO_4$, 0.01 M EDOT was prepared. As EDOT fairly soluble in organic solvents, no sonication was required. Polymerization carried out potentiodynamically in a three electrode system by cycling the potential onto desired electrodes at 0.005 $V \cdot s^{-1}$ from -0.455 V to 1.3 V vs. Ag/AgCl (saturated KCl) reference electrode and a platinum flag as the counter electrode. For this experiment PEDOT deposited simultaneously by shorting all four band electrodes together. After 12 successive cycles a dark film growth observed. Figure 1 b in supplementary information shows image of band electrodes before and after deposition of PEDOT and current response of 12 successive scans during deposition process. After deposition, the films were conditioned (redox cycled 3/4 times) in monomer free solution. This conditioning or stabilization increases the reproducibility of electrochemical responses.[81] After conditioning, the electrodes were ready for characterization.

2.3.5. Poly(3,4-ethylenedioxythiophene (PEDOT) characterization

Magnetohydrodynamic pumping is proportional to electronic current that generates from a fixed geometry of cell and electrode in a particular electrolyte solution. So, current responses in various electrolyte solutions will be a good predictor of possible fluid speed in MHD pumping. Cyclic voltammetry (CV) and Chronoamperommetry (CA) were used as characterization techniques for PEDOT film. CV was done in 0.1 M KCl with bare electrodes and for PEDOT coated electrodes

for comparison purpose. Figure 4 in supplementary information shows CV responses for only one electrode in 0.1 M KCl solution which has a shape of double layer charging current with 813 times more current with PEDOT coated electrode than the bare electrode. This increase in current with PEDOT confirms large improvement in MHD pumping. CA and integrated CA responses (Chronocoulometry or CP, Figure 3 in supplementary information) in 60 % Phosphate buffer saline + 40% glycerol solution shows maximum current and charge at the time length of 20 sec. In MHD pumping how far and at what speed fluid will flow will depend on the supply of charge and ease of ion transportation the film which can be determined by charge and current density form CA and integrated CA data in a particular solution.

2.3.6. Axial resolution of optical setup

To measure the axial resolution of the system, the Barrier filter was removed and a mirror (Newport, Irvine, CA) was placed at the beam waist of the light sheet. The mirror was then translated 30 µm above and below the convergence of the beam waist in 0.5 µm increments while taking an image at each interval to measure the amount of light throughput outside of the focal plane. This was done with two different magnifications of 10x and 20x and three binning modes to yield detection apertures of 5, 10, and 20 µm. The theoretical axial resolution was determined to be 9.47 and 3.26 µm for the 10x (0.3 NA) and 20x (0.5 NA) objectives, respectively. These values were determined by applying Equation 1, which shows that the driving factors of axial resolution are excitation wavelength, numerical aperture of the objective, and refractive index. The method of utilizing a slit aperture has been previously described and is stated that the linear sensor does not need to be modelled to a theoretical equation considering a slit or pinhole aperture.[35]

Equation 1.

$$Resolution_{axial} = \frac{0.89 * n * \bar{\lambda}}{(n - \sqrt{n^2 - NA^2})}$$

2.3.7. Agarose bead phantom for qualitative imaging study

Agarose (Sigma Aldrich, St. Louis, MO) was mixed in distilled water at 5% (w/v) and heated in a microwave to create a dense ring to contain the core of the phantom for imaging. The core of the phantom was then mixed at 3% (w/v) agarose in distilled water and the total was mixed with 15 µm fluorescent polystyrene microspheres. This three-dimensional solution of microspheres was placed under the e-LSCM and used to qualitatively demonstrate the optical sectioning.

2.3.8. Solution preparation for imaging in redox-MHD

Fluorescent polystyrene microspheres were used to ensure image quality and aspect ratio. 800 µl of beads were prepared by spinning out of solution and resuspension in a 60 to 40 solution of PBS and 50% glycerol in H_2O, respectively. This solution had a 20% absolute glycerol concentration to enable neutral buoyancy of the beads in a deep gasket. A polydimethyl siloxane (PDMS) gasket of 2.14 mm height and with a cutout of 3 cm x 1.8 cm was placed on the chip, and the solution was then dispensed into the well. A 24 × 50 mm, #1.5 coverslip (VWR, Radnor, PA) was then placed on top of the PDMS gasket to seal the well for imaging. The entire system was placed on the platform along with the edge connector (Category S28626, Sullins Connector Solution, CA) which was connected to a galvanostat (760B CH instrument, Arlington , TX).

2.3.9. Correlations of linear speed as a result of applied current in a sealed chamber

Linear speeds of fluorescent beads were determined by MHD study in a sealed chamber. Four band electrodes on the chip was modified with PEDOT and of them two electrodes (1 and 2) were selected for pumping. A 2.14 mm thick PDMS (Polydimethylsiloxane) gasket with a 3 cm × 1.8 cm rectangular opening defined the cell dimensions by providing sidewalls (Figure 2a in supplementary information). A glass coverslip (VWR micro cover glass, 1 ounce, 24 × 50 mm) was placed directly over the gasket as a ceiling of the cell which also limit the vertical direction of fluid flow. 1100 µL solution of 60 % PBS + 40 % glycerol solution with $5x10^4$ polystyrene fluorescent beads was added into the cell. Figure 2b in supplementary information shows that the chip connected with edge connector, gasket, and coverslip on it, was placed over a 0.37 T NdFeB cylindrical permanent magnet (diameter of 1.5 in. and height of 0.5 in.; Amazing Magnets LLC, Irvine, CA) so as magnet was centered over the active band electrodes (used for pumping). Chronopotentiometry (CP) experiment was performed for MHD flow where one band electrode (E 1) was used as working and adjacent band electrode (E 2) used as combined counter/quasi-reference electrode. Current applied from 150 µA to 750 µA with 120 µA stepping in between the electrodes with a cutoff voltage of 1.1 V. To track the flow of the solution around the PEDOT modified electrodes fluorescent beads (FluoSpheres, Thermo Fisher scientific) were added into the solution and visualized and recorded with a Sony Handycam (HDR-XR 500 V) interfaced with a microscope (Leica DM 2500 M). The focusing height above the chip surface was adjusted by lowering and raising of the microscope objective. The quantification of fluid speed was acquired by processing the bead movement in the recorded videos by tracking individual bead with particle tracking software (WIM, WWW.PHYSICSTOOLKIT.COM). Bead speed was determined

by tracking six individual beads over a given amount of time when current was applied in low to high, high to low and random fashion at 480 µm and 1440 µm above the chip surface.

2.3.10. Synchronization of applied current and line period for image quality assurance

As we determined the linear speeds as a function of applied current, we quantified image quality as a function of drive current. We have previously demonstrated the importance of synchronization with the linear sensor and a push broom scanning source.[79] The camera's acquisition parameters were set to 300 µs line period and an internally controlled exposure time of 12.5 µs to eliminate image saturation. With this line period, we started at a low applied current of 350 µA and increased it in intervals of 50 µA to determine the influence on image quality. Image quality was quantified in post-processing with ImageJ (Broad Institute, USA); it was defined by aspect ratio of the bead. Aspect ratio, in this context, has been set as the height to the width of the bead. The ratio is equal to one if the bead is geometrically circular which ensures that the line period is matched to the linear speed.

2.3.11. Sample preparation for imaging leukocytes

Whole blood was drawn via venipuncture in accordance with IRB protocol at the University of Arkansas. Red blood cells were then lysed in accordance with a custom protocol using ammonium chloride lysing solution. The fragments were removed and leukocytes washed in PBS / 0.1% (w/v) BSA (Sigma-Aldrich, St. Louis, MO) and stained in a 1:1 dilution of acridine orange dye (20 µg mL^{-1}). The staining dye was then removed from solution, and the product was re-suspended in 600:400 µL PBS / glycerol (50/50 in distilled water).

2.4. Results and Discussion

As was previously stated, axial resolution is variable upon refractive index, numerical aperture, and the average of the excitation and emission wavelengths. Since, for the purposes of the proposed system, the wavelengths are consistent and only objectives with air as a refractive medium are used, the influence of numerical aperture was experimentally demonstrated with a 10x (0.3 NA) and 20x (0.5 NA). Figure 11 shows the experimentally determined axial resolution of the two mentioned objectives and the quantification of these curves are defined as the full width half maximum (FWHM). The FWHM is the width of the curve at half of the normalized maximum. The experimental FWHM for all binning modes and magnifications are reported in Table 2 and correlated to the respective theoretical value for that objective. The justification for one theoretical calculation per objective has been previously demonstrated when using a linear aperture [35]; this method of using binning modes for an adjustable aperture is novel so there is limited theoretical precedence for this approach.

TABLE 2. Full width half maximum measurements

	10x, 0.3 NA		*20x, 0.5 NA*	
Aperture	*Theoretical*	*Experimental*	*Theoretical*	*Experimental*
5 µm	9.5 µm	13.5 µm	3.3 µm	4.5 µm
10 µm		14.0 µm		4.9 µm
20 µm		14.75 µm		6.25 µm

For all images taken for a respective objective the laser power and acquisition parameters were held static to demonstrate the light throughput increase at different binning modes. The smaller the allowed aperture, the finer the axial resolution, and the axial resolution sees consistent divergence based upon the aperture width. A significant divergence in the quality of axial resolution is also seen, as expected, in the change of numerical aperture. Figure 12 (a-f) also shows a qualitative test of microspheres in agarose to demonstrate the quantitative experimental measurements shown in Table 2. The slight increase in background signal based upon increased aperture width is commensurate to the FWHM values observed, as well as with the more significant increase in background signal due to decrease in numerical aperture.

For each set of applied current two beads were analyzed giving a total of six beads for speed analysis. Figure 10a shows linearity of bead speed with applied current with error bar in speed direction at two different height on the chip. The data was collected by current applied in high to low, low to high and random fashion for reproducibility assurance. Bead speed analysis at 480 µm and 1440 µm above the chip surface shows maximum speed of 1395 ± 32.4 µm/s and 1818.33 ± 55 µm/s at applied current of 750 µA. Bead speed is linear to the current applied regardless the order of the application with R^2 value of 0.9971 and 0.9974 at two different height on the chip. This linear dependency confirms the consistency of previous study which has done with solution redox species and bare electrodes.[80, 82] Different bead speeds were observed at different position over the chip at the same applied current. Increased applied current (i.e. higher speed) consumes total charge from PEDOT film faster, hence fluid flows shorter distance (short duration) but with high speed. Figure 10b shows the correlation between applied current and total time of MHD flow where the maximum flow time (61.6 ± 1.2 s) obtained by applying lowest current (150

μA) and least flow time (10.4 ± 0.3 s) obtained with maximum applied current (750 μA). So depending upon the application a particular speed and flow time can be obtained with a certain applied current which will allow better programmability of the MHD device. Figure 13 show the convergence of aspect ratio at one at 850 μA while the line exposure period was set to 300 μsec; this synchronization will ensure image quality when using these technologies for broader applications. Figure 13 also shows microspheres imaged with the e-LSCM within the R-MHD chamber using the specified parameters determined by the previous experiment to show qualitative assurance of realistic aspect ratio. Figure 14 demonstrates this platform's ability for high-resolution imaging of biological samples by showing three types of leukocytes; these cells were imaged with the e-LSCM in the R-MHD chamber.

2.5. Conclusions

In conclusion, we present a redox-magnetohydrodynamic microfluidic device with an epitaxial light sheet confocal microscope for high-resolution imaging of biological specimens toward an image cytometer with limited reagent preparation. The deep well of R-MHD allows no solution clogging from dense cellular population, high linear speeds, and large sample volumes; this interfaces well with the optical sectioning of the e-LSCM to image in the midst of bulk fluid flow. The e-LSCM has fast, intermediate data transfer rates which makes it ideal for imaging objects at high speeds with the ability to transfer and process images at a separate computing unit which could be of use for image algorithm process flow. The optical setup provides a novel design in confocal fluorescence microscopy by eliminating a mechanical slit and utilizing pixel binning modes for an adjustable aperture. The combination of the precise, flat flow profiles of R-MHD and confocal alignment of a linear sensor allows this system no moving parts. The complementary

nature of this system with the broad range of biomedical application makes it an attractive diagnostic platform for dissemination at the point-of-care.

2.6. Supplementary Information

Supporting information is placed in Appendix B includes the electrode chip design, electrochemical response during deposition of PEDOT film, device setup while doing the MHD study, Chronoamperometric and chronocoulometric response of electrode with PEDOT film, comparative CV response in an electrolyte solution before and after PEDOT deposition.

3. CONCLUSIONS

3.1. Summary

Image cytometry has been discussed as a robust tool to monitor cell populations by image analysis algorithms. Image cytometry builds on the premise of high throughput machinery introduced by flow cytometry, the industry standard. This method builds on this premise by complementing it with myriad imaging techniques for a more comprehensive classification capability. It is more comprehensive because it can add insight into the source of the signal from within the cell population which has the potential for extended intuition into the population beyond a limited data point, for example fluorescence intensity. This insight is in particular useful for tracking dysplasia, general cellular abnormality, since many times the phenotypic markers of disease progression are unknown. These markers could be present at many places within the population or intra-cellular itself, and image analysis can provide more data to these questions. There are many different imaging techniques which can be used to tailor toward different applications, the imaging technique here is an epitaxial light sheet confocal microscope (e-LSCM).

A linear sensor is used in this study to image objects in motion. These sensors are attractive to eliminate motion blur of fast moving objects as they acquire lines (portions of a scene) at a time as the object moves across the sensor, transfer them intermittently to a central computing unit, and then concatenate them in post-acquisition. Intermittent data transfer allows these linear sensors to have rapid acquisition and shorter exposure periods which combats motion blur when imaging moving objects, while comparable speeds have been achieved by some two-dimensional arrays, linear sensors can bypass the extensively complex sensor architecture needed for these area sensors.

The linear sensor in this study was also used as a confocal aperture able to block out of focus light in the epitaxial configuration without the need of a pinhole or slit, used in conventional confocal microscopy; this ability allows the microscope to tailor to different applications. For example, in this study, optical sectioning was used to image within a 2 mm well microfluidic device, whereas before using optical sectioning the images would have had a signal to background ratio too low to yield useful data. This complemented the R-MHD device (electro-chemical microfluidic platform) well due to the fact that increasing the well height reduces drag force and overall pressure which yields higher linear speeds, this, in turn, can potentially increase throughput of this image cytometer. The R-MHD device can also hold more fluid with the deeper well which also potentially increases the throughput of this image cytometer.

Along with the benefits that the e-LSCM, the use of a microfluidic device for push broom translation allows the elimination of scanning optics (i.e. acousto-optical beam deflectors and galvanometers). Push broom translation also complements the continuous field of view available to the linear sensor. The coupling of these technologies presents novel mechanical findings, but it also allows for myriad diagnostic applications as the platform is not tailored to any one test.

Altogether, this study proposes the combination of two technologies which complement well for a multi-faceted approach. This study combines epitaxial light sheet confocal microscopy and electro-chemical microfluidics as a robust approach to image cytometry all while simplifying the mechanics by eliminating a slit, utilizing no moving parts and offering a continuous field of view.

3.2. Future Directions

3.2.1. Blood cell classification into a three-part differential

The future directions of this project are broad but work is being done to classify blood cells into a three-part differential (lymphocytes, granulocytes, and monocytes); this is a relatively basic but influential place to start as flow cytometers have made themselves indispensable to clinics and physicians in diagnosing blood disorders and monitoring chemotherapy induced myelosupression.[83-85] Work has begun studying a common dye, acridine orange, used for lab-on-chip system tailored to diagnosing blood disorders.[86, 87] Acridine orange is an amphipathic vital which intercalates DNA and RNA content depending on the electrostatical intracellular interactions of the cell which can also be due to a change in pH levels.[88] The type of biological content that it intercalates then determines what wavelength it emits while still absorbing efficiently in the blue region of the spectrum; this diverse Stokes shift allows a cheap, simple diagnostic test for classifying different blood cells.[89] In this study, it has been detected that the cells exhibit a slight red shift over a short period of time after staining (5-6 minutes); this could be problematic since the three-part differential is calculated by the per-cell red to green ratio (R:G ratio). The above proposed platform has been investigated as an attractive approach to rapidly image these cells before this red shift. We are now optimizing an image algorithm based upon machine learning by imaging these blood cells with a whole slide scanning technique; this techniques mimics the recent shift to digital histopathology analysis.[90-92] Along with training the algorithm, it has also been demonstrated that we can yield high-resolution blood cell images with the e-LSCM and the R-MHD technique outlined in this paper (Figure 14).

3.2.2. Different microfluidic patterns for sorting and filtering in biomedical applications

The proposed R-MHD device has previously demonstrated the ability to drive fluid in an array of patterns, individually addressed electrodes to direct objects in opposite directions, a flat flow

profile which can aid many diagnostic tests, and recently, immobilized redox species patterned onto the electrodes which is attractive for biological cell analysis.[80, 82, 93-95] These microfluidic manipulations present an attractive platform for biomedical applications especially that of specialized tests at the point of care. By coupling these capabilities to the proposed optical methods, a procedural problem is being addressed by sorting and filtering clustered cell isolates. A consistently published area of recent is the issue of organoid growths *in vitro* for genomic testing, drug efficacy, and heterogeneous cell populations.[96-100] These organoids can be formed from whole tissue, malignant growths, treated tissues, biopsies, and myriad number of other forms.[97, 101-103] The successful growth of these three-dimensional *in vitro* growths typically depends on the efficiency of isolating pure populations containing clusters of cells which carry pluripotent stem cell able to self-replicate.[104] The microfluidic manipulation capabilities mentioned along with the above proposed image cytometry approach could provide an attractive platform to sort and filter isolates of many cell populations derived from extracted tissues. This application has potential impact in a wide range of biomedical research by providing a practical solution to a procedural inefficiency.

3.2.3. Utilizing the simplified mechanical components for potential dissemination at the point of care

The coupling of these technologies presents novel mechanical findings, but it also allows for myriad diagnostic applications as the platform is not tailored to any one test. Altogether, this study proposes the combination of two technologies which complement well for a multi-faceted approach. This study combines epitaxial light sheet confocal microscopy and electro-chemical microfluidics as a robust approach to image cytometry all while simplifying the mechanics by

eliminating a slit, utilizing no moving parts and offering a continuous field of view. The simplification of these mechanical properties can yield an attractive point of care device for multi-form diagnostic tests. The potential for compartmentalization toward mobile, remote diagnostic applications is in concurrence with recent research to take medical services to low resource areas.[86, 89, 105-107]

REFERENCES

1. Porichis, F., et al., *High-throughput detection of miRNAs and gene-specific mRNA at the single-cell level by flow cytometry.* Nature communications, 2014. **5**.

2. Poncelet, P., et al., *Standardized counting of circulating platelet microparticles using currently available flow cytometers and scatter-based triggering: Forward or side scatter?* Cytometry Part A, 2015.

3. Standerholen, F.B., et al., *Comparison of electronic volume and forward scatter principles of cell selection using flow cytometry for the evaluation of acrosome and plasma membrane integrity of bull spermatozoa.* Cytometry Part A, 2014. **85**(8): p. 719-728.

4. Birchler, A., et al., *Seamless Combination of Fluorescence-Activated Cell Sorting and Hanging-Drop Networks for Individual Handling and Culturing of Stem Cells and Microtissue Spheroids.* Analytical chemistry, 2016.

5. Julius, M., T. Masuda, and L. Herzenberg, *Demonstration that antigen-binding cells are precursors of antibody-producing cells after purification with a fluorescence-activated cell sorter.* Proceedings of the National Academy of Sciences, 1972. **69**(7): p. 1934-1938.

6. Bisi, J.E., et al., *Preclinical Characterization of G1T28: A Novel CDK4/6 Inhibitor for Reduction of Chemotherapy-induced Myelosuppression.* Molecular cancer therapeutics, 2016: p. molcanther. 0775.2015.

7. Arnold, D.M., et al., *Approach to the diagnosis and management of drug-induced immune thrombocytopenia.* Transfusion medicine reviews, 2013. **27**(3): p. 137-145.

8. Upreti, D., A. Pathak, and S.K. Kung, *Development of a standardized flow cytometric method to conduct longitudinal analyses of intracellular CD3ζ expression in patients with head and neck cancer.* Oncology Letters, 2016. **11**(3): p. 2199-2206.

9. Shang, Y.-J., et al., *Systematic review and meta-analysis of flow cytometry in urinary tract infection screening.* Clinica Chimica Acta, 2013. **424**: p. 90-95.

10. Nedosekin, D.A., et al., *In vivo photoswitchable flow cytometry for direct tracking of single circulating tumor cells.* Chemistry & biology, 2014. **21**(6): p. 792-801.

11. Ithimakin, S., et al., *HER2 drives luminal breast cancer stem cells in the absence of HER2 amplification: implications for efficacy of adjuvant trastuzumab.* Cancer research, 2013. **73**(5): p. 1635-1646.

12. Datta, J., et al., *Anti-HER2 CD4+ T-helper type 1 response is a novel immune correlate to pathologic response following neoadjuvant therapy in HER2-positive breast cancer.* Breast Cancer Res, 2015. **17**(1): p. 71.

13. Mao, X., et al., *An integrated, multiparametric flow cytometry chip using "microfluidic drifting" based three-dimensional hydrodynamic focusing.* Biomicrofluidics, 2012. **6**(2): p. 024113.

14. Lapsley, M.I., L. Wang, and T.J. Huang, *On-chip flow cytometry: where is it now and where is it going?* Biomarkers in medicine, 2013. **7**(1): p. 75-78.

15. Cheng, Y., et al., *High-throughput and clogging-free microfluidic filtration platform for on-chip cell separation from undiluted whole blood.* Biomicrofluidics, 2016. **10**(1): p. 014118.

16. Shields IV, C.W., C.D. Reyes, and G.P. López, *Microfluidic cell sorting: a review of the advances in the separation of cells from debulking to rare cell isolation.* Lab on a Chip, 2015. **15**(5): p. 1230-1249.

17. Cheng, I.-F., et al., *Antibody-free isolation of rare cancer cells from blood based on 3D lateral dielectrophoresis.* Lab on a Chip, 2015. **15**(14): p. 2950-2959.

18. Carpenter, A.E., et al., *CellProfiler: image analysis software for identifying and quantifying cell phenotypes.* Genome biology, 2006. **7**(10): p. R100.

19. Dolfi, S.C., et al., *The metabolic demands of cancer cells are coupled to their size and protein synthesis rates.* Cancer Metab, 2013. **1**(20): p. 10.1186.

20. MacAulay, C., et al., *High throughput image cytometry for detection of suspicious lesions in the oral cavity.* Journal of biomedical optics, 2012. **17**(8): p. 0860041-08600411.

21. Blasi, T., et al., *Label-free cell cycle analysis for high-throughput imaging flow cytometry.* Nature communications, 2016. **7**.

22. Brakenhoff, G. and K. Visscher, *Confocal imaging with bilateral scanning and array detectors.* Journal of microscopy, 1992. **165**(1): p. 139-146.

23. Higgins, L.M., et al., *Line-scanning confocal microscopy for high-resolution imaging of upconverting rare-earth-based contrast agents.* Journal of biomedical optics, 2015. **20**(11): p. 110506-110506.

24. Kino, G.S. and T.R. Corle, *Confocal scanning optical microscopy and related imaging systems*. 1996: Academic Press.

25. Wolleschensky, R., B. Zimmermann, and M. Kempe, *High-speed confocal fluorescence imaging with a novel line scanning microscope.* Journal of biomedical optics, 2006. **11**(6): p. 064011-064011-14.

26. Greger, K., J. Swoger, and E. Stelzer, *Basic building units and properties of a fluorescence single plane illumination microscope.* Review of Scientific Instruments, 2007. **78**(2): p. 023705.

27. Deschout, H., et al., *On-chip light sheet illumination enables diagnostic size and concentration measurements of membrane vesicles in biofluids.* Nanoscale, 2014. **6**(3): p. 1741-1747.

28. Basiji, D.A., et al., *Cellular image analysis and imaging by flow cytometry.* Clinics in laboratory medicine, 2007. **27**(3): p. 653-670.

29. Heo, H.-P. and S.-W. Ra, *Reducing Motion Blur by Adjusting Integration Time for Scanning Camera with TDI CMOS.* International Journal of Signal Processing Systems, 2015. **3**(2).

30. Shoushun, C., F. Boussaid, and A. Bermak, *Robust intermediate read-out for deep submicron technology CMOS image sensors.* Sensors Journal, IEEE, 2008. **8**(3): p. 286-294.

31. De Franchis, C., et al., *Attitude Refinement for Orbiting Pushbroom Cameras: a Simple Polynomial Fitting Method.* Image Processing On Line, 2015. **2015**: p. 328-361.

32. Kartofelev, D., et al. *Application of high-speed line scan camera for string vibration measurements*. in *Proceedings of International Symposium on Musical Acoustics (ISMA 2014), Le Mans, France*. 2014.

33. Van Wolputte, S., et al. *Embedded line scan image sensors: The low cost alternative for high speed imaging*. in *Image Processing Theory, Tools and Applications (IPTA), 2015 International Conference on*. 2015: IEEE.

34. Wong, C.-W. and K.-K. Chong, *Solar flux distribution study of non-imaging dish concentrator using linear array of triple-junction solar cells scanning technique.* Solar Energy, 2016. **125**: p. 86-98.

35. Mei, E., et al., *A line scanning confocal fluorescent microscope using a CMOS rolling shutter as an adjustable aperture.* Journal of microscopy, 2012. **247**(3): p. 269-276.

36. Yang, Z., et al., *Dual-slit confocal light sheet microscopy for in vivo whole-brain imaging of zebrafish.* Biomedical optics express, 2015. **6**(5): p. 1797-1811.

37. Tchernykh, V., et al. *Airborne test results for smart pushbroom imaging system with optoelectronic image correction*. in *Remote Sensing*. 2004: International Society for Optics and Photonics.

38. Jacobsen, K., *Calibration of imaging satellite sensors.* Int. Arch. Photogramm. Remote Sensing, 2006. **36**: p. 1.

39. Poglitsch, A., et al., *The photodetector array camera and spectrometer (PACS) on the Herschel space observatory.* Astronomy & astrophysics, 2010. **518**: p. L2.

40. Chung, A.J. and S.C. Hur, *High-Speed Microfluidic Manipulation of Cells.* Micro-and Nanomanipulation Tools, 2015.

41. Lau, A.K., et al., *Ultrafast Microfluidic Cellular Imaging by Optical Time-Stretch.* Imaging Flow Cytometry: Methods and Protocols, 2016: p. 23-45.

42. Mohan, K. and P.P. Mondal, *Light sheet based imaging flow cytometry on a microfluidic platform.* Microscopy research and technique, 2013. **76**(11): p. 1101-1107.

43. Stevens, M., et al., *High-resolution dosimetry using radiochromic film and a document scanner.* Physics in medicine and biology, 1996. **41**(11): p. 2357.

44. Al-Janobi, A. *Color line scan system for grading date fruits*. in *ASAE Annual International Meeting*. 1998.

45. Heiss-Czedik, D., et al., *Demosaicing algorithms for area-and line-scan cameras in print inspection.* Journal of Visual Communication and Image Representation, 2009. **20**(6): p. 389-398.

46. Fischer, J. and T. Radil, *DSP based measuring line-scan CCD camera.* Proceedings of IDAACS, 2003: p. 345-348.

47. Ross, W.N., et al., *Imaging with organic indicators and high-speed charge-coupled device cameras in neurons: some applications where these classic techniques have advantages.* Neurophotonics, 2014. **2**(2): p. 021005-021005.

48. Wang, B., et al. *Performances of a solid streak camera based on conventional CCD with nanosecond time resolution*. in *The International Conference on Photonics and Optical Engineering and the Annual West China Photonics Conference (icPOE 2014)*. 2015: International Society for Optics and Photonics.

49. Reich, R., et al., *High-speed, electronically shuttered solid-state imager technology.* Review of scientific instruments, 2003. **74**(3): p. 2027-2031.

50. Li, Y.-S., T.Y. Young, and C.-C. Huang, *Noncontact measurement using line-scan cameras: Analysis of positioning error.* Industrial Electronics, IEEE Transactions on, 1989. **36**(4): p. 545-551.

51. Bodenstorfer, E., et al. *High-speed line-scan camera with digital time delay integration*. in *Proc. SPIE, Real-Time Image Processing 2007* 2007.

52. Jeong, H.-W., et al., *High-speed dual-beam, crossed line-scanning fluorescence microscope with a point confocal resolution.* Applied Optics, 2015. **54**(12): p. 3811-3816.

53. Pierna, J.A.F., et al., *Line scan hyperspectral imaging spectroscopy for the early detection of melamine and cyanuric acid in feed.* Journal of Near Infrared Spectroscopy, 2014. **22**(2): p. 103-112.

54. Fechtig, D.J., et al., *Line-field parallel swept source MHz OCT for structural and functional retinal imaging.* Biomedical optics express, 2015. **6**(3): p. 716-735.

55. Hirata, M., et al., *Macular choroidal thickness and volume in normal subjects measured by swept-source optical coherence tomography.* Investigative ophthalmology & visual science, 2011. **52**(8): p. 4971-4978.

56. Tal, E., D. Oron, and Y. Silberberg, *Improved depth resolution in video-rate line-scanning multiphoton microscopy using temporal focusing.* Optics letters, 2005. **30**(13): p. 1686-1688.

57. Macedo, M. and C. Correia. *Development and assessment of image reconstruction algorithms using a low-cost bench-microscope based on a linear CMOS image sensor*. in *European Conferences on Biomedical Optics*. 2009: International Society for Optics and Photonics.

58. Macedo, M.P., et al. *Modeling of image formation of a low-cost white-light bench microscope with a linear CMOS image sensor: its application in metrology*. in *Proc. SPIE, Modeling Aspects in Optical Metrology*. 2007. Munich, Germany.

59. Yang, T., et al., *Rapid imaging of large tissues using high-resolution stage-scanning microscopy.* Biomedical optics express, 2015. **6**(5): p. 1867-1875.

60. Bravo-Zanoguera, M.E., et al., *Dynamic autofocus for continuous-scanning time-delay-and-integration image acquisition in automated microscopy.* Journal of Biomedical Optics, 2007. **12**(3): p. 034011-034011-16.

61. Canali, C., et al., *Bioimpedance monitoring of 3D cell culturing—Complementary electrode configurations for enhanced spatial sensitivity.* Biosensors and Bioelectronics, 2015. **63**: p. 72-79.

62. Shadfan, B.H., et al., *A multiplexable, microfluidic platform for the rapid quantitation of a biomarker panel for early ovarian cancer detection at the point-of-care.* Cancer Prevention Research, 2015. **8**(1): p. 37-48.

63. Karabacak, N.M., et al., *Microfluidic, marker-free isolation of circulating tumor cells from blood samples.* Nature protocols, 2014. **9**(3): p. 694-710.

64. Srinivasan, V., V.K. Pamula, and R.B. Fair, *An integrated digital microfluidic lab-on-a-chip for clinical diagnostics on human physiological fluids.* Lab on a Chip, 2004. **4**(4): p. 310-315.

65. Tangen, U., et al., *On demand nanoliter-scale microfluidic droplet generation, injection, and mixing using a passive microfluidic device.* Biomicrofluidics, 2015. **9**(1): p. 014119.

66. Weston, M.C., M.D. Gerner, and I. Fritsch, *Magnetic fields for fluid motion.* Analytical chemistry, 2010. **82**(9): p. 3411-3418.

67. Fritsch, I. *Microfluidics with Alternating Current-Redox Magnetohydrodynamics at Modified Electrodes for Cell Identification*. in *227th ECS Meeting (May 24-28, 2015)*. 2015: Ecs.

68. Xia, Y. and G.M. Whitesides, *Soft lithography.* Annual review of materials science, 1998. **28**(1): p. 153-184.

69. Prieto, S.P., et al., *Proflavine Hemisulfate as a Fluorescent Contrast Agent for Point-of-Care Cytology.* PloS one, 2015. **10**(5).

70. Pierce, M.C., et al., *Accuracy of in vivo multimodal optical imaging for detection of oral neoplasia.* Cancer Prevention Research, 2012. **5**(6): p. 801-809.

71. Skala, M.C., et al., *Multiphoton microscopy of endogenous fluorescence differentiates normal, precancerous, and cancerous squamous epithelial tissues.* Cancer research, 2005. **65**(4): p. 1180-1186.

72. Hutcheson, J.A., et al. *High-throughput microfluidic line scan imaging for cytological characterization*. in *SPIE BiOS*. 2015: International Society for Optics and Photonics.

73. Gordonov, S., et al., *Time series modeling of live-cell shape dynamics for image-based phenotypic profiling.* Integrative Biology, 2016. **8**(1): p. 73-90.

74. Cerignoli, F., et al., *High throughput measurement of Ca 2+ dynamics for drug risk assessment in human stem cell-derived cardiomyocytes by kinetic image cytometry.* Journal of pharmacological and toxicological methods, 2012. **66**(3): p. 246-256.

75. Al-Janabi, S., A. Huisman, and P.J. Van Diest, *Digital pathology: current status and future perspectives.* Histopathology, 2012. **61**(1): p. 1-9.

76. Grant, K.M., J.W. Hemmert, and H.S. White, *Magnetic field-controlled microfluidic transport.* Journal of the American Chemical Society, 2002. **124**(3): p. 462-467.

77. Leventis, N. and X. Gao, *Magnetohydrodynamic electrochemistry in the field of Nd-Fe-B magnets. Theory, experiment, and application in self-powered flow delivery systems.* Analytical chemistry, 2001. **73**(16): p. 3981-3992.

78. Anderson, E.C., M.C. Weston, and I. Fritsch, *Investigations of redox magnetohydrodynamic fluid flow at microelectrode arrays using microbeads.* Analytical Chemistry, 2010. **82**(7): p. 2643-2651.

79. Hutcheson, J.A., et al., *A widefield fluorescence microscope with a linear image sensor for image cytometry of biospecimens: Considerations for image quality optimization.* Review of Scientific Instruments, 2015. **86**(9): p. 093709.

80. Sahore, V. and I. Fritsch, *Flat Flow Profiles Achieved with Microfluidics Generated by Redox-Magnetohydrodynamics.* Analytical Chemistry, 2013. **85**(24): p. 11809-11816.

81. Hillman, A.R., S.J. Daisley, and S. Bruckenstein, *Solvent effects on the electrochemical p-doping of PEDOT.* Physical Chemistry Chemical Physics, 2007. **9**(19): p. 2379-2388.

82. Weston, M.C. and I. Fritsch, *Manipulating fluid flow on a chip through controlled-current redox magnetohydrodynamics.* Sensors and Actuators B: Chemical, 2012. **173**: p. 935-944.

83. Stachurski, D., et al., *Flow cytometric analysis of myelomonocytic cells by a pattern recognition approach is sensitive and specific in diagnosing myelodysplastic syndrome and related marrow diseases: emphasis on a global evaluation and recognition of diagnostic pitfalls.* Leukemia research, 2008. **32**(2): p. 215-224.

84. Boesen, J.J., K. Nooter, and D. Valerio, *Circumvention of chemotherapy-induced myelosuppression by transfer of themdr1 gene.* Biotherapy, 1993. **6**(4): p. 291-302.

85. Hallek, M., et al., *Guidelines for the diagnosis and treatment of chronic lymphocytic leukemia: a report from the International Workshop on Chronic Lymphocytic Leukemia updating the National Cancer Institute–Working Group 1996 guidelines.* Blood, 2008. **111**(12): p. 5446-5456.

86. Forcucci, A., et al. *Design and Fabrication of Miniature Objective Lens for Three Part White Blood Cell Differential Measurements*. in *Bio-Optics: Design and Application*. 2015: Optical Society of America.

87. Denes, V., et al., *Metastasis blood test by flow cytometry: In vivo cancer spheroids and the role of hypoxia.* International Journal of Cancer, 2015. **136**(7): p. 1528-1536.

88. McMaster, G.K. and G.G. Carmichael, *Analysis of single-and double-stranded nucleic acids on polyacrylamide and agarose gels by using glyoxal and acridine orange.* Proceedings of the National Academy of Sciences, 1977. **74**(11): p. 4835-4838.

89. Chu, K., Z.J. Smith, and S. Wachsmann-Hogiu, *Development of inexpensive blood imaging systems: where are we now?* Expert review of medical devices, 2015. **12**(5): p. 613-627.

90. Ordi, J., et al., *Validation of whole slide imaging in the primary diagnosis of gynaecological pathology in a University Hospital.* Journal of clinical pathology, 2015. **68**(1): p. 33-39.

91. Beckwith, B.A., *Standards for Digital Pathology and Whole Slide Imaging*, in *Digital Pathology*. 2016, Springer. p. 87-97.

92. Mercan, E., et al., *Localization of Diagnostically Relevant Regions of Interest in Whole Slide Images: a Comparative Study.* Journal of digital imaging, 2016: p. 1-11.

93. Henry, C.S. and I. Fritsch, *Microfabricated recessed microdisk electrodes: characterization in static and convective solutions.* Analytical chemistry, 1999. **71**(3): p. 550-556.

94. Henry, C.S. and I. Fritsch, *Microcavities containing individually addressable recessed microdisk and tubular nanoband electrodes.* Journal of the Electrochemical Society, 1999. **146**(9): p. 3367-3373.

95. Nash, C.K. and I. Fritsch, *Poly (3, 4-ethylenedioxythiophene)-Modified Electrodes for Microfluidics Pumping with Redox-Magnetohydrodynamics (MHD): Improving Compatibility for Broader Applications by Eliminating Addition of Redox Species to Solution.* Analytical Chemistry, 2015.

96. Ranga, A., N. Gjorevski, and M.P. Lutolf, *Drug discovery through stem cell-based organoid models.* Advanced drug delivery reviews, 2014. **69**: p. 19-28.

97. Walsh, A.J., et al., *Drug response in organoids generated from frozen primary tumor tissues.* Scientific reports, 2016. **6**.

98. Matano, M., et al., *Modeling colorectal cancer using CRISPR-Cas9-mediated engineering of human intestinal organoids.* Nature medicine, 2015. **21**(3): p. 256-262.

99. Zalatan, J.G., et al., *Engineering complex synthetic transcriptional programs with CRISPR RNA scaffolds.* Cell, 2015. **160**(1): p. 339-350.

100. Walsh, A.J., et al., *Quantitative optical imaging of primary tumor organoid metabolism predicts drug response in breast cancer.* Cancer research, 2014. **74**(18): p. 5184-5194.

101. Mahe, M.M., et al., *Establishment of Human Epithelial Enteroids and Colonoids from Whole Tissue and Biopsy.* Journal of visualized experiments: JoVE, 2015(97).

102. Ohta, Y. and T. Sato, *Intestinal tumor in a dish.* Frontiers in medicine, 2014. **1**.

103. Sato, T., et al., *Long-term expansion of epithelial organoids from human colon, adenoma, adenocarcinoma, and Barrett's epithelium.* Gastroenterology, 2011. **141**(5): p. 1762-1772.

104. Huch, M. and B.-K. Koo, *Modeling mouse and human development using organoid cultures.* Development, 2015. **142**(18): p. 3113-3125.

105. Cogan, D., *The development of low cost autonomous chemical sensors for environmental monitoring*. 2015, Dublin City University.

106. DIVE, G.D., *Sensing Impacts: Remote Monitoring using Sensors.* 2016.

107. Gulari, M.N., *An optofluidic lens biochip and an x-ray readable blood pressure microsensor: versatile tools for in vitro and in vivo diagnostics*. 2015, The University of Michigan.

APPENDIX A. FIGURES

Intro Figure 1.

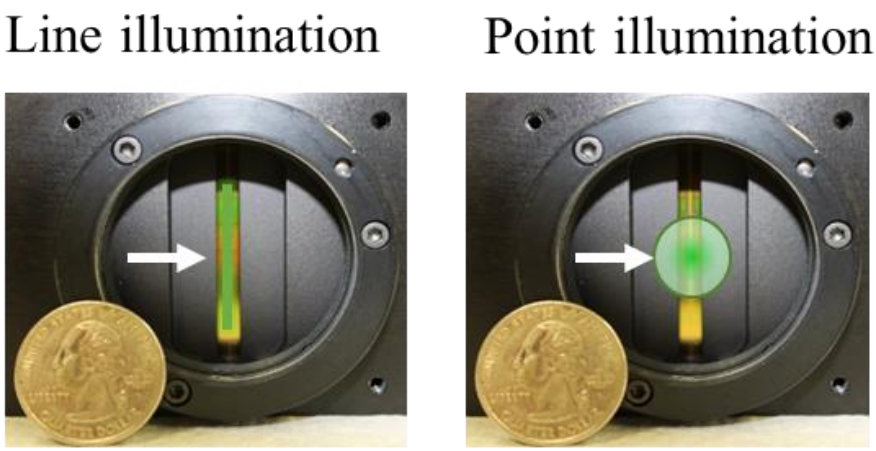

Intro Figure 2.

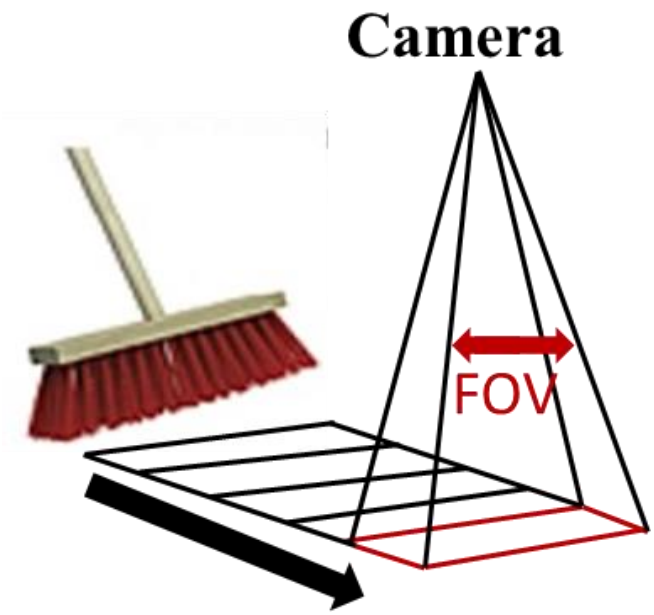

Figure 1.

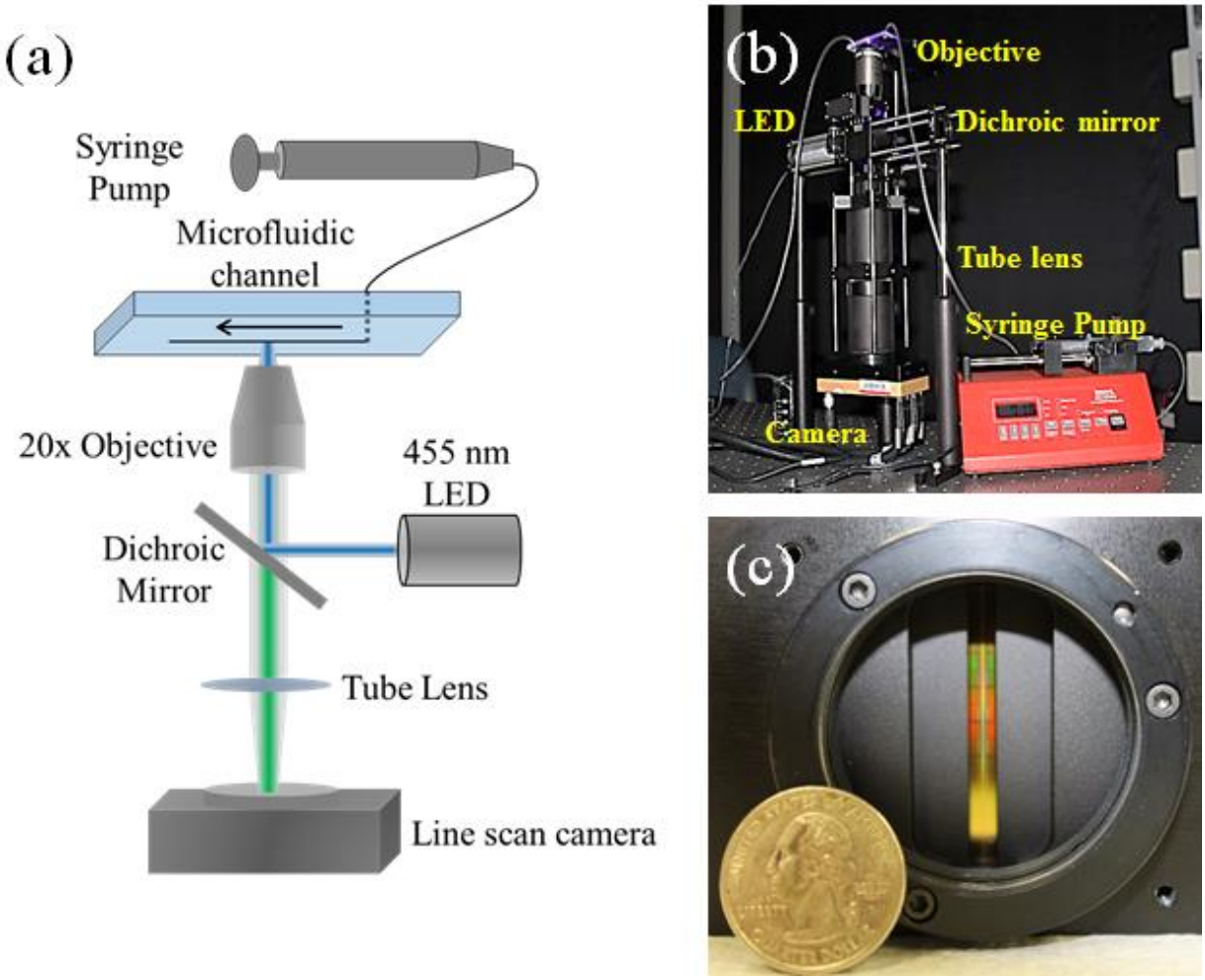
(a)
Syringe Pump
Microfluidic channel
20x Objective
455 nm LED
Dichroic Mirror
Tube Lens
Line scan camera
(b)
Objective
LED
Dichroic mirror
Tube lens
Syringe Pump
Camera
(c)

Figure 2.

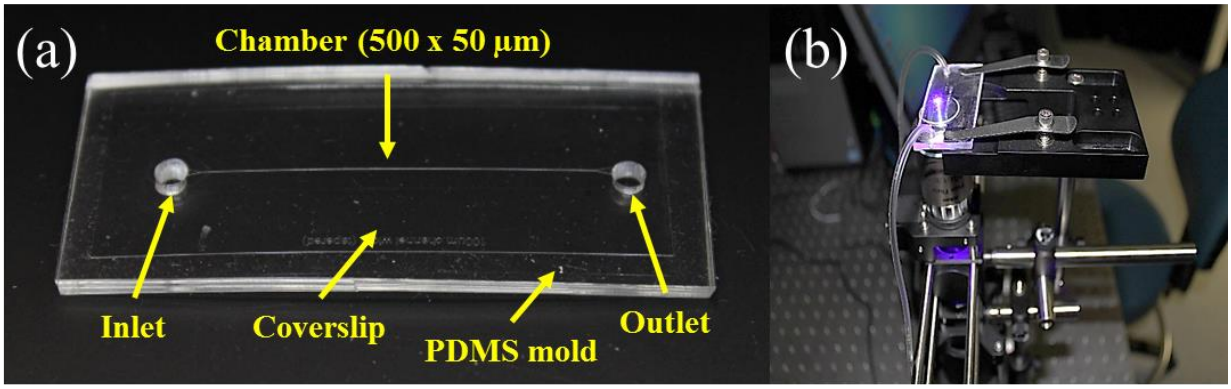

Figure 3.

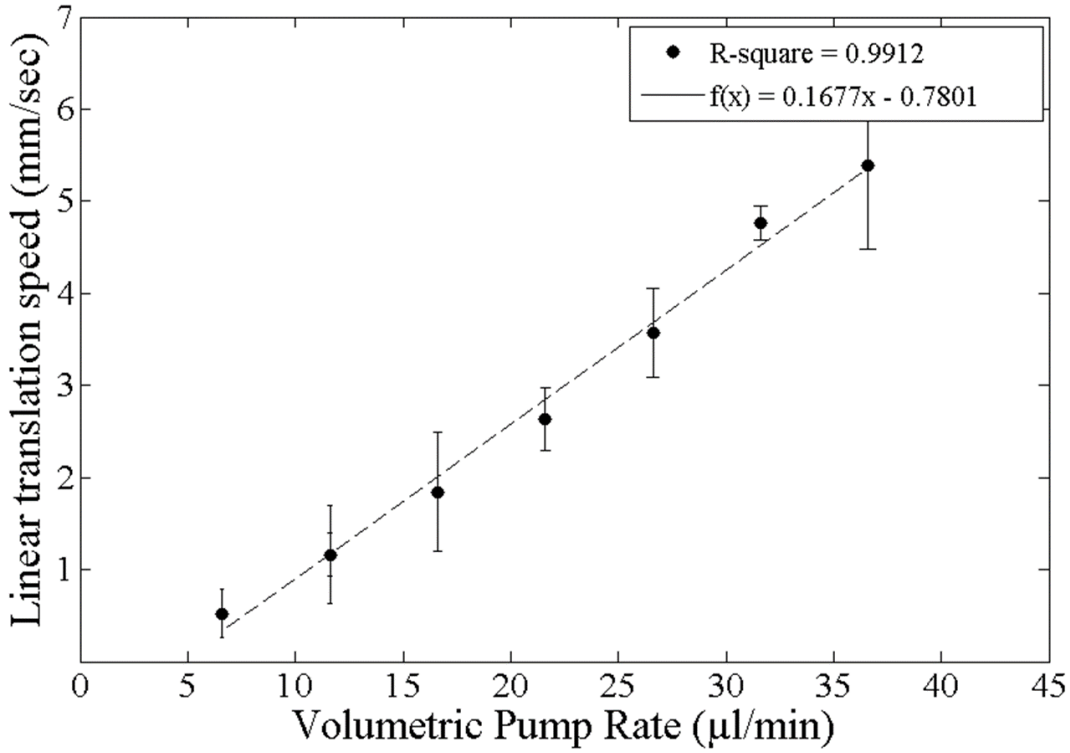
R-square = 0.9912
f(x) = 0.1677x - 0.7801
Linear translation speed (mm/sec)
Volumetric Pump Rate (µl/min)
0
5
10
15
20
25
30
35
40
45
1
2
3
4
5
6
7

Figure 4.

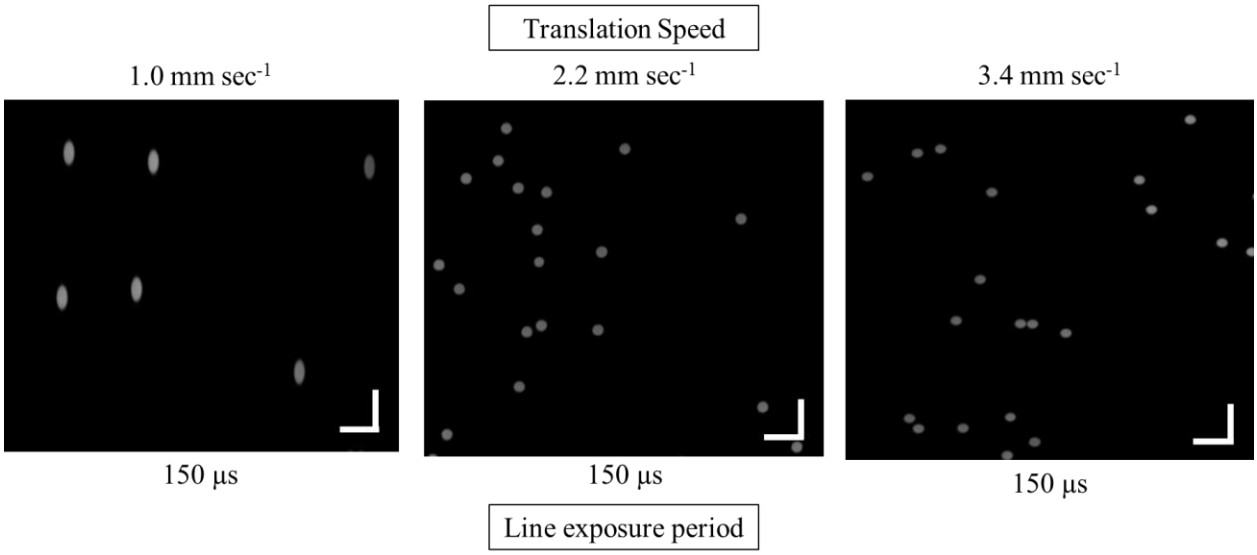
Translation Speed
1.0 mm sec-1
2.2 mm sec-1
3.4 mm sec-1
150 µs
150 µs
150 µs
Line exposure period

Figure 5.

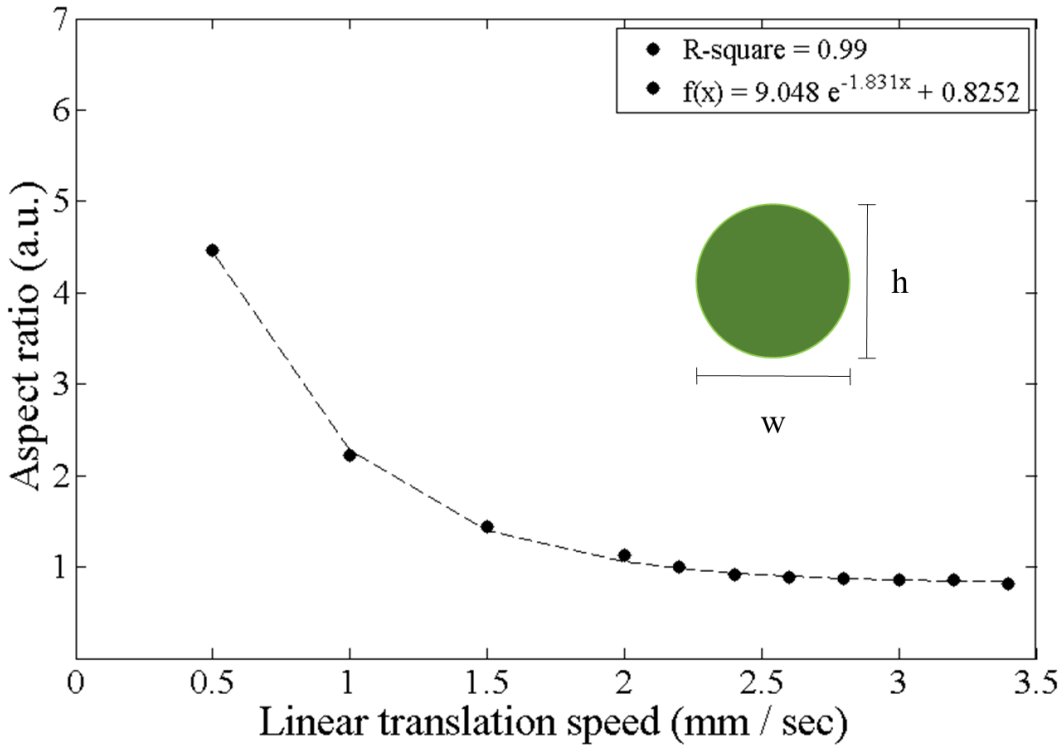
R-square = 0.99
f(x) = 9.048 e^-1.831x + 0.8252
h
w
Aspect ratio (a.u.)
Linear translation speed (mm / sec)
0
0.5
1
1.5
2
2.5
3
3.5
1
2
3
4
5
6
7

Figure 6.

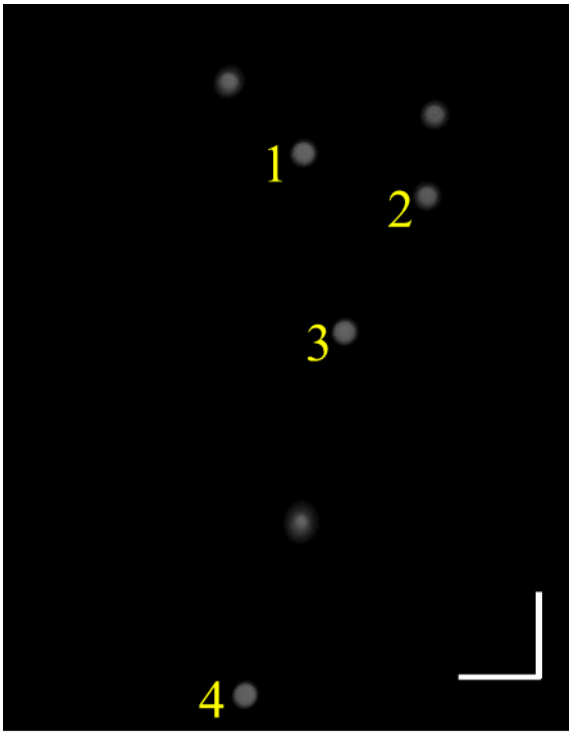

Figure 7.

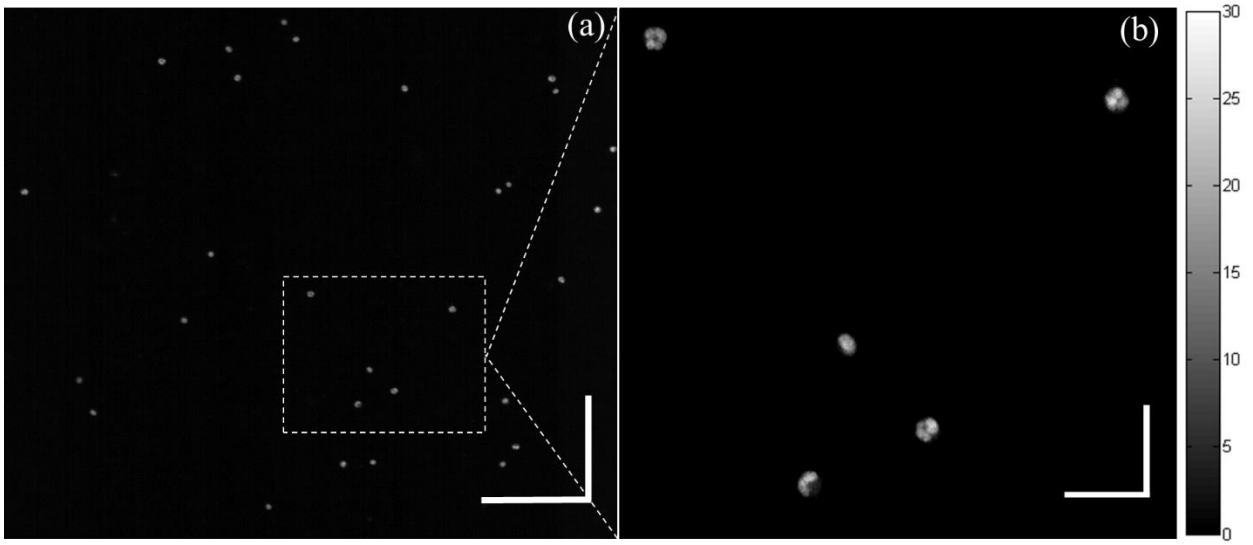

Figure 8.

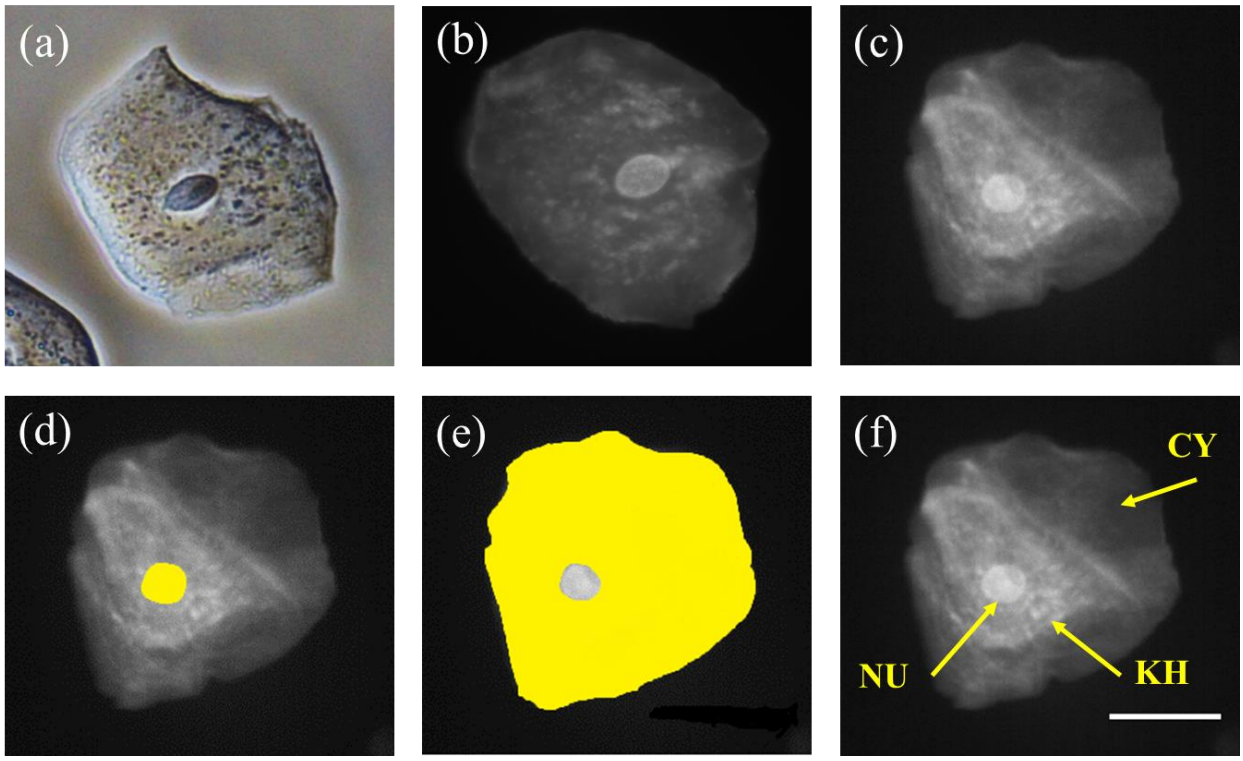

Figure 9.

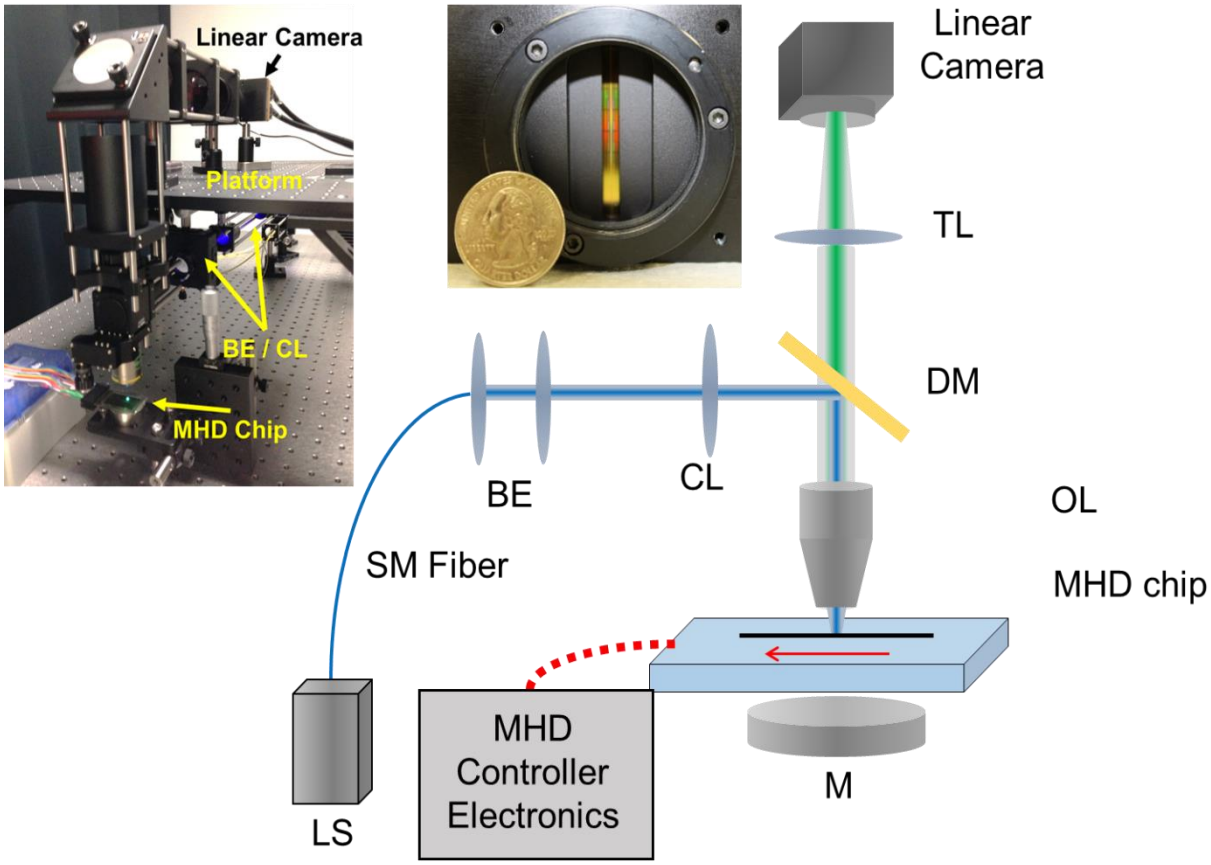
Linear Camera
Platform
BE / CL
MHD Chip
Linear Camera
TL
DM
BE
CL
OL
SM Fiber
MHD chip
MHD Controller Electronics
M
LS

Figure 10.

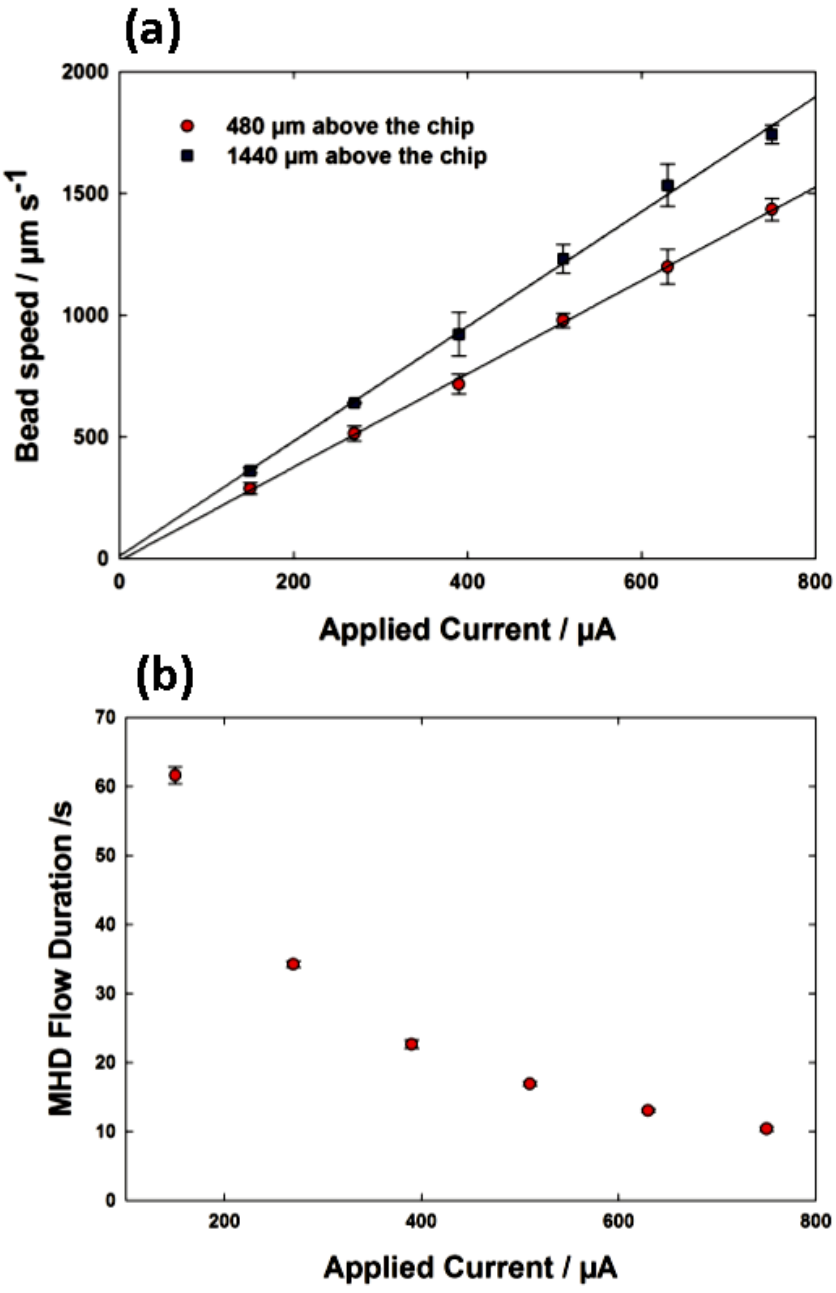
(a)
480 µm above the chip
1440 µm above the chip
Bead speed / µm s-1
Applied Current / µA
(b)
MHD Flow Duration /s
Applied Current / µA

Figure 11.

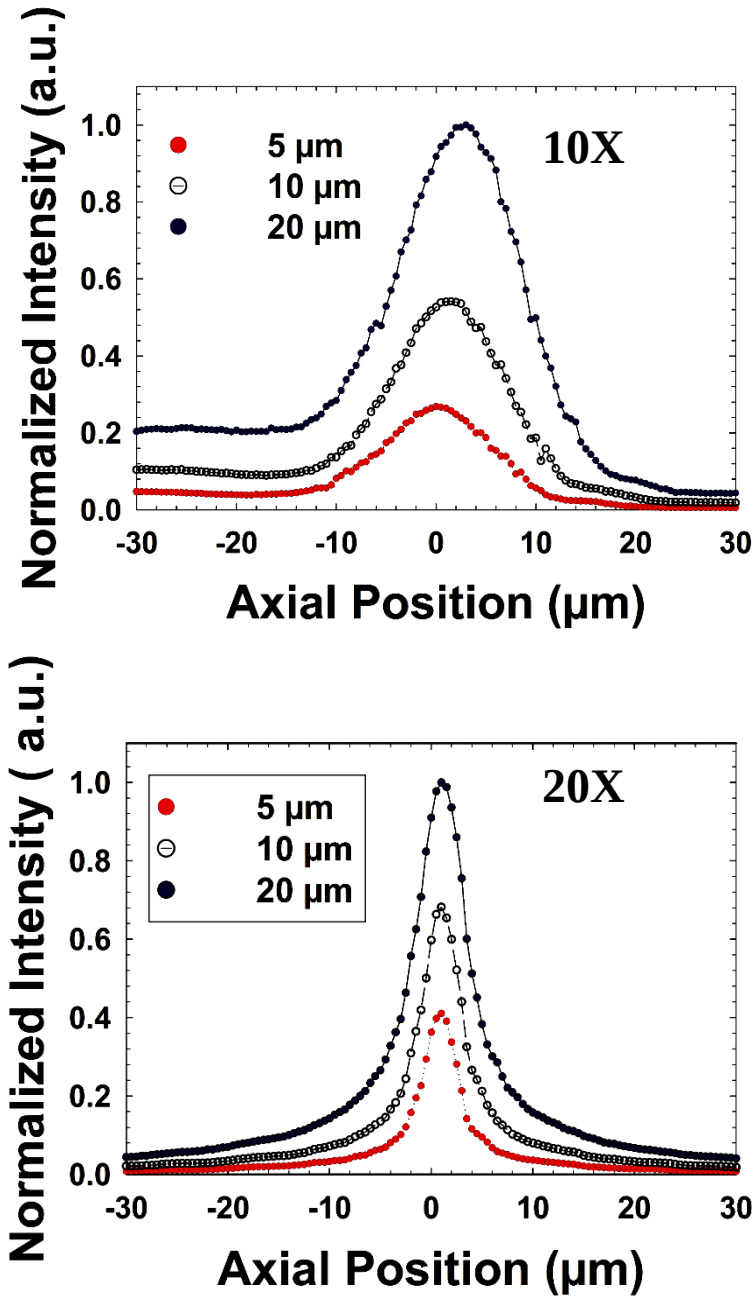
Normalized Intensity (a.u.)
1.0
0.8
0.6
0.4
0.2
0.0
5 µm
10 µm
20 µm
10X
-30
-20
-10
0
10
20
30
Axial Position (µm)
Normalized Intensity (a.u.)
1.0
0.8
0.6
0.4
0.2
0.0
5 µm
10 µm
20 µm
20X
-30
-20
-10
0
10
20
30
Axial Position (µm)

Figure 12.

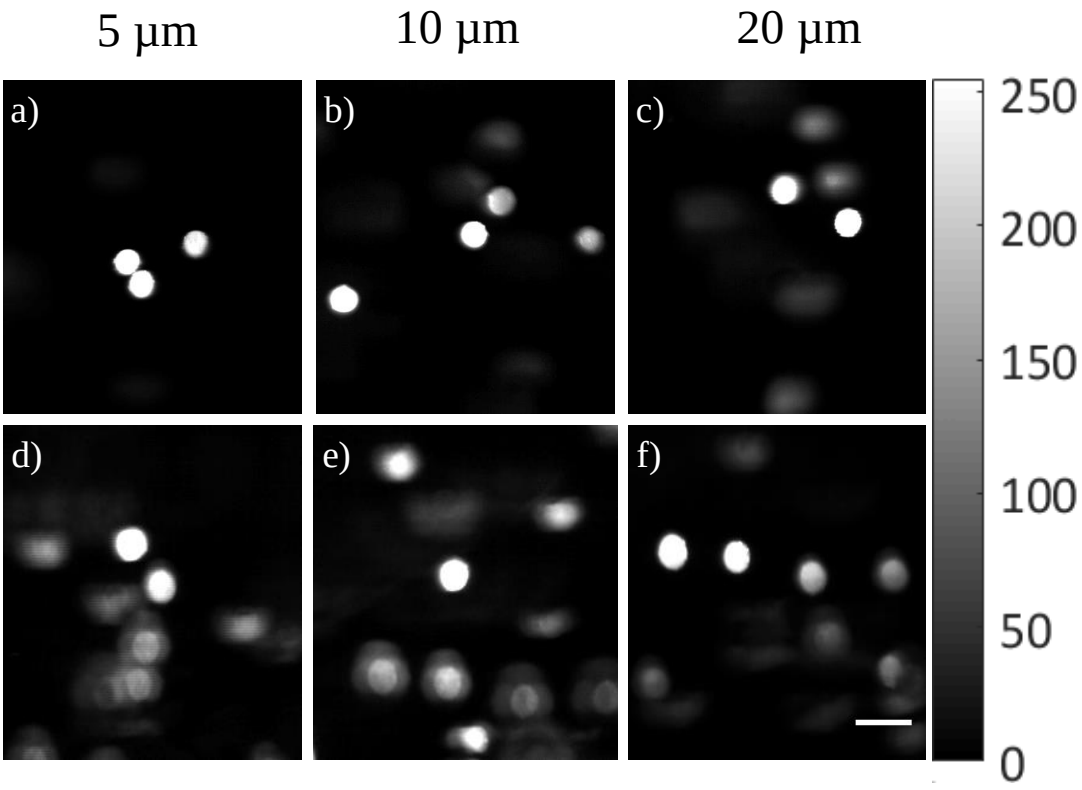

Figure 13.

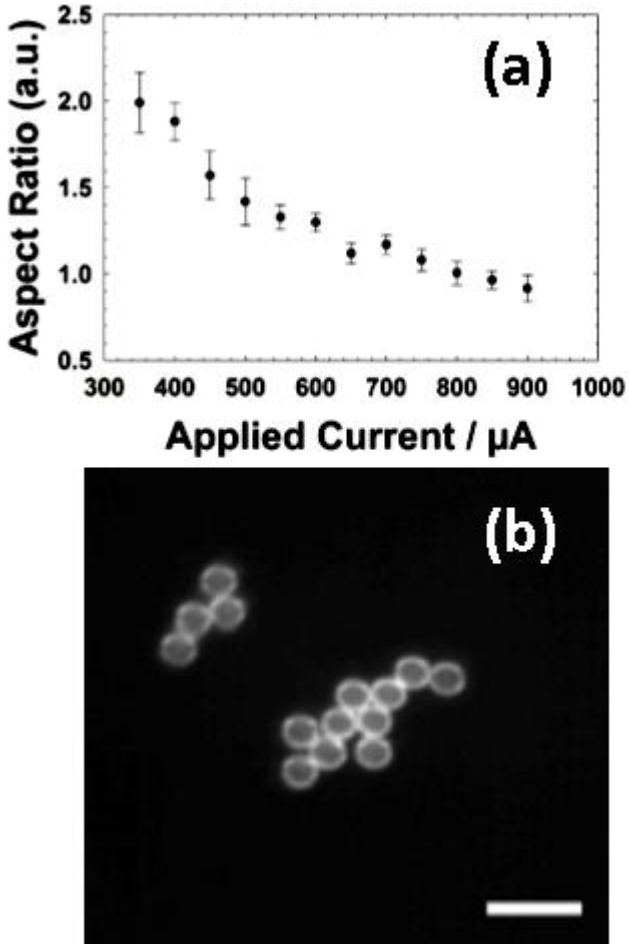
(a)
Aspect Ratio (a.u.)
2.5
2.0
1.5
1.0
0.5
300
400
500
600
700
800
900
1000
Applied Current / μA
(b)

Figure 14.

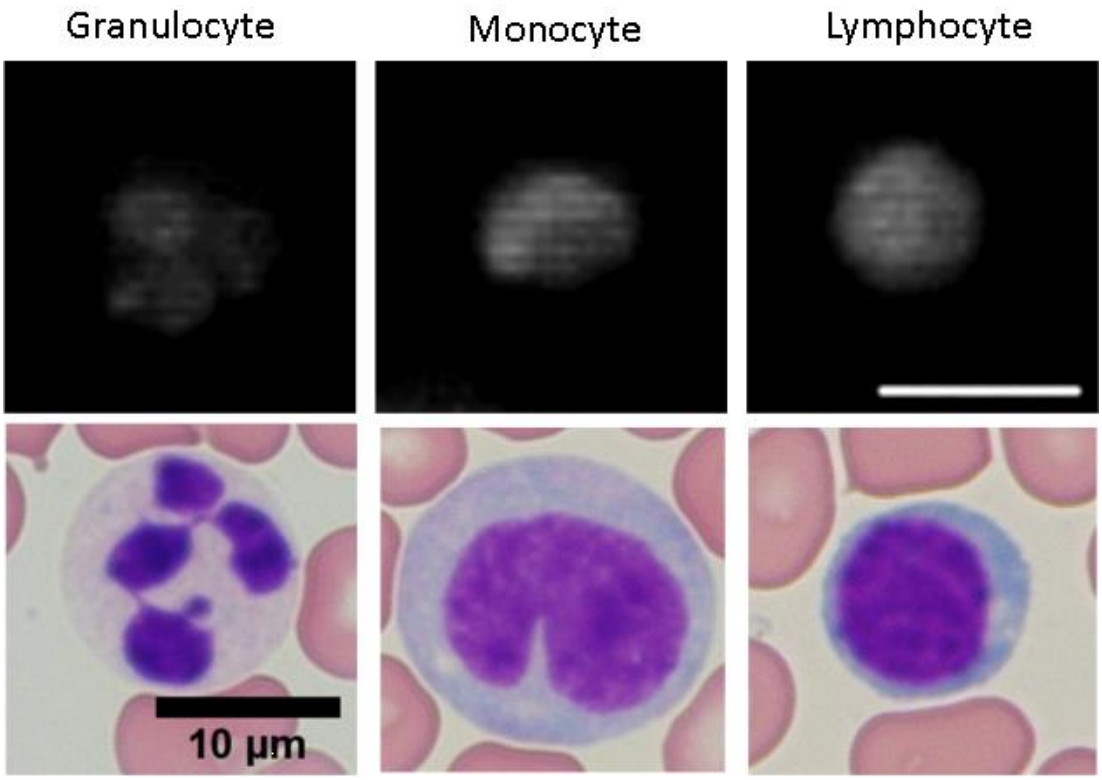

APPENDIX B. SUPPLEMENTARY INFORMATION

SI Figure 1.

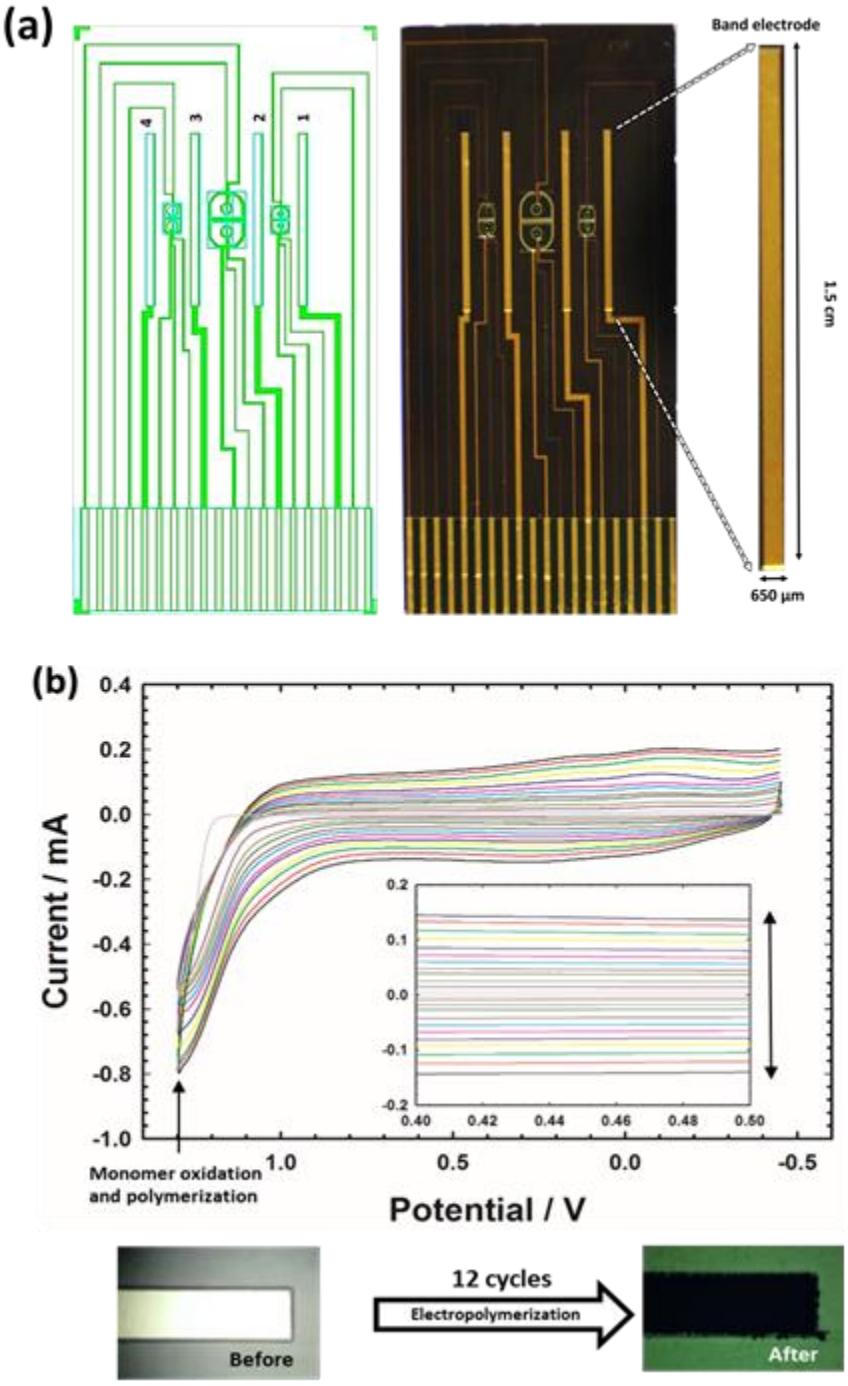

SI Figure 2.

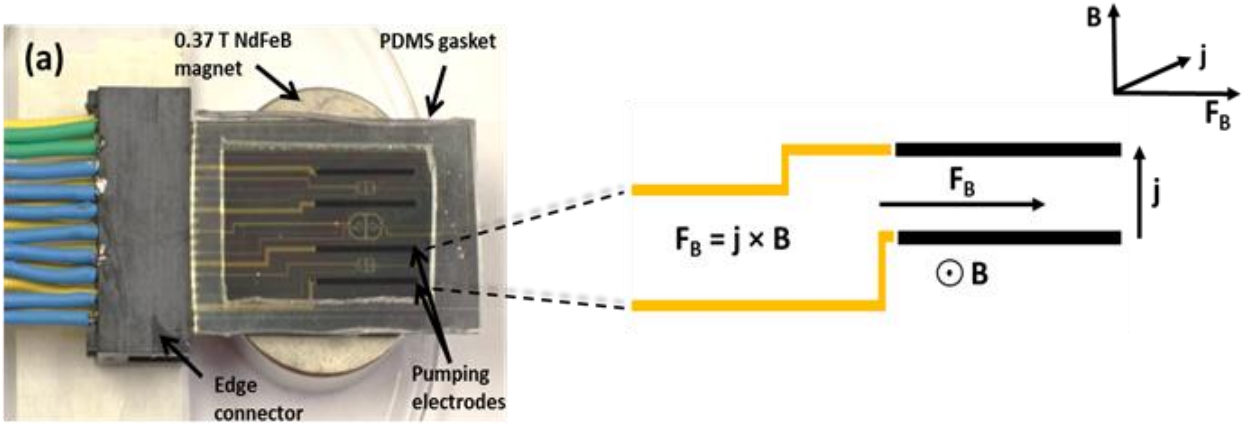
(a)
0.37 T NdFeB magnet
PDMS gasket
Edge connector
Pumping electrodes
B
j
F_B
F_B = j × B
⊙ B

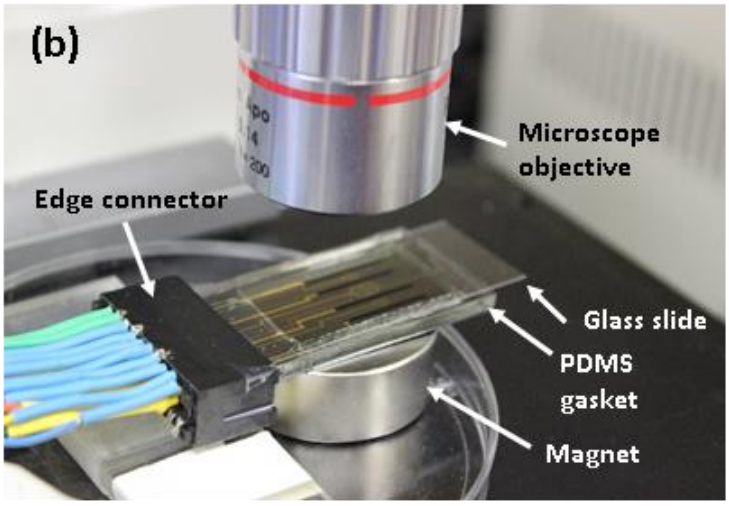
(b)
Microscope objective
Edge connector
Glass slide
PDMS gasket
Magnet

SI Figure 3.

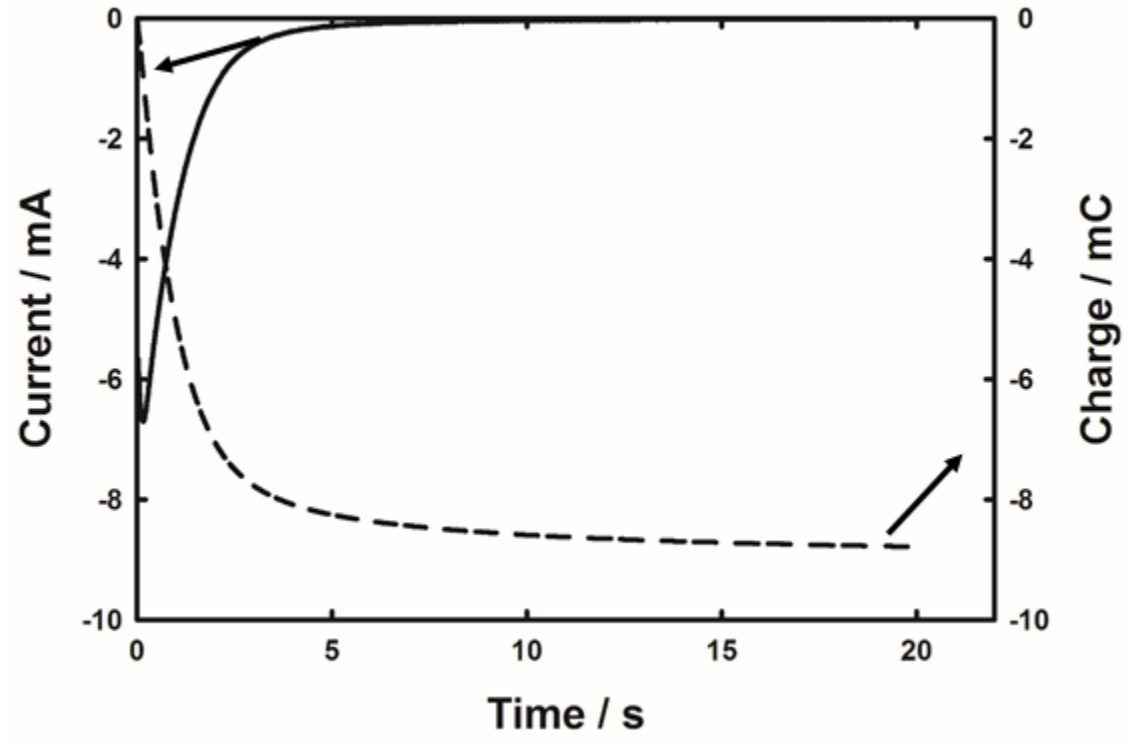

SI Figure 4.

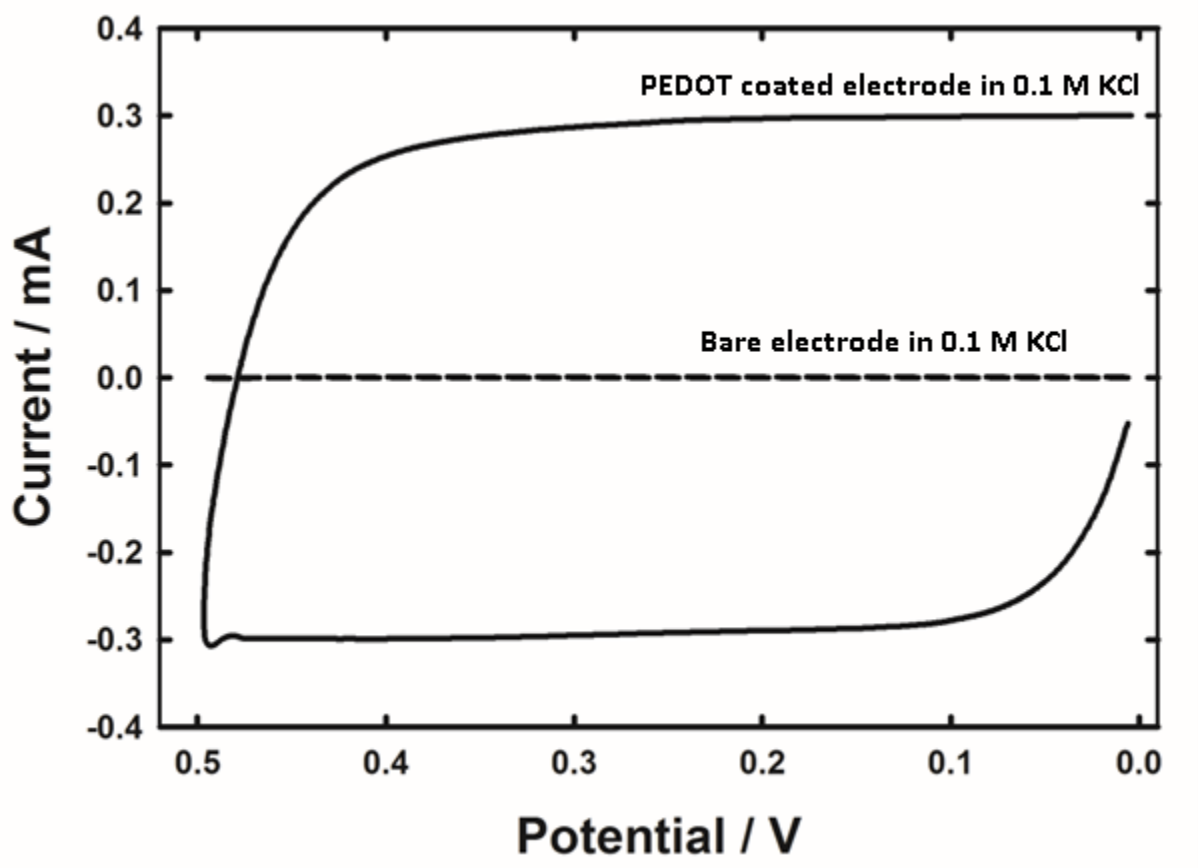
PEDOT coated electrode in 0.1 M KCl
Bare electrode in 0.1 M KCl
Current / mA
Potential / V
0.4
0.3
0.2
0.1
0.0
-0.1
-0.2
-0.3
-0.4
0.5
0.4
0.3
0.2
0.1
0.0